Revista Mexicana de Física **43**, *No. 4 (1997) 545–591*

Self-affine properties of fracture surfaces

ALEXANDER S. BALANKIN AND FRANCISCO J. SANDOVAL
Instituto Tecnológico y de Estudios Superiores de Monterrey
Campus Estado de México, Mexico

Recibido el 4 de junio de 1996; aceptado el 10 de octubre de 1996

ABSTRACT. A statistical topography of fracture surfaces is discussed. Theoretical models of fracture surfaces and experimental methods of fractal measurements are analyzed. The theoretical ideas which allow to understand the strong contradictions between results obtained by different authors in studies of fracture surfaces morphology are presented. Suggested theoretical concepts are discussed with respect to experimental observations reported in the literature. A fractal analysis of brittle fracture surfaces in steel type 1045, fractured at different temperatures, is reported.

RESUMEN. Este trabajo presenta la topografía estadística de las superficies de fractura por medio del análisis de modelos teóricos y métodos experimentales de medición fractal. Son presentados también los argumentos teóricos que permiten entender las fuertes contradicciones en diferentes estudios de superficies de fractura obtenidas por diferentes autores. Los conceptos teóricos sugeridos son discutidos con referencia a las observaciones experimentales reportadas en la literatura. Finalmente se presenta un análisis fractal de las superficies de fractura frágil para el acero 1045 a diferentes temperaturas.

PACS: 62.20Mk; 05.45.+b; 47.53.+n

1. INTRODUCTION

Fracture surfaces morphologies represent a complex mosaic of microstructural artifacts, the features of which are characteristic of the particular fracture mode and microstructure and may range in size from the atomic dimensions of dislocation slip steps to the macroscopic dimensions of grain size [1–4]. An understanding of this morphology requires the deconvolution of these characteristic dimensions, which together form the building blocks of the fracture surface. Characteristic fracture dimensions are related to significant microstructural length which influence the specific local micromechanisms of fracture [2–7]. For this reason, in recent years, the quantitative analysis of fractured surfaces has become an integral part of the study of deformation and rupture of materials [1–3]. Such surface analysis often provide information about surface morphology which is complementary to that obtained by other metallurgical methods. Starting from the pioneer work of Mandelbrot *et al.* [8] there have been numerous investigations focusing on the crack faces morphology characterization within a framework of fractal geometry, that is believed to give a promising parameters in establishing a property-structure relationships (see, for review Refs. 3–32 and references therein). It is now clearly established that at the first view the random fracture patterns can be treated as fractal objects.

The application of fractal geometry provides an effective tool in the study of highly irregular fracture surfaces. Many different materials have been investigated, with different fracture behavior from ductile to brittle, at a very different scales from nanometer scale using atomic force or scanning tunneling microscopy [3, 33], micrometer to centimeter scale using profilometry measurements on a variety of materials [3, 34], image analysis techniques [3, 8, 35] or other techniques [3, 36], meter [37] and up to kilometer scale [18] for geological faults. The initial hope in measuring the surface topography was to relate this geometrical information to mechanical properties, such as toughness [3, 9, 10, 39, 40], energy release rate [9, 10, 41], tensile strength [3, 42], impact energy [3, 8], fatigue threshold value of ΔK_{th} [43], ductility [42, 44, 45], and Weibul's moduli [6, 46–48], or to material characterization [1–3, 42]. However, some technical difficulties are related to the determination of the fractal properties of real fracture surfaces which are statistically self-affine rather than statistically self-similar (see Refs. 9, 10 and references therein). Because of this, some commonly used tools which were developed for isotropic fractals lead to biased measurements. As a result we have strong contradictions between results obtained in different studies (see, for example, Refs. 9, 10, 33, 49–51 and references therein). In practice, these contradictions give arguments to the traditional metallurgist concerning the non-utility of using fractal geometry concepts to describe fracture in materials.

The main goal of present study is to understand the reasons and the nature of the aforementioned contradictions in results of different investigations. For this purpose the previously published data on fractal characterization of fracture surfaces as well as different experimental techniques are analyzed.

Some new concepts are also suggested to fractal characterization of fracture surfaces. These concepts are validated by the analysis of different fractal patterns. Furthermore, as an example, the fractal properties of brittle fracture surfaces in steel type 1045, fractured in standard mechanical tests at different temperatures, are also studied.

2. STATISTICAL TOPOGRAPHY OF FRACTURE SURFACES

The quantitative characterization and modeling of fracture surface roughness is an important problem for both theoretical and applied fracture mechanics. Traditional techniques, based on the idea of isolated deviations from planar surface geometry (*e.g.*, a facet of an elemental solid with occasional steps and kinks), face the difficulty of identifying a small number of structural parameters that can describe the roughness for a wide variety of purposes. Typically they depend on a multitude of model-specific parameters difficult to access in practice. Fractal geometry, developed by Mandelbrot [52], allows the description of such irregular forms which are more complex than Euclidean shapes. More recently there have been extensive research and great development in statistical topography which now acts as an integral part of the quantitative fractography [1–3].

The term "statistical topography" was introduced by Ziman [53] for the theory of the shapes of random fields, with special emphasis on the contour lines and surfaces of a random potential. A mathematical survey of the statistical topography of Gaussian random fields was given by Adler [54]. The descriptions of scaling invariance are of crucial importance for statistical topography.

The most compelling example of statistical topography is presented by the diverse and whimsical patterns of natural coastlines and islands. The geographical considerations apparently inspired Mandelbrot [52] to introduce the concept of fractals. Generally speaking, the fractal analysis provides a description of how space is occupied by a particular shape or curve. Specifically, the fractal dimension (which is commonly fractional in the contrast to the topological dimension which can be only an integer) measures the relative amount of detail or "roughness" occurring over a range measurement intervals. The more tortuous, convoluted and richer in details the shape, the higher fractal (metric) dimension.[1]

In mathematics, "fractal" and its fractal (metric) dimension, D, both are defined in terms of an embedding metric space. Some of the most important definitions of the metric dimension are given in Table I. Intuitively one can interpret metric (fractal) dimension, D, as the smallest non-negative real number for which one can define a volume form on n-dimensional Euclidean space which is not identically zero; such a volume form being entirely described by the metric dimension or capacity. Underlining this approach is the recognition that one and two-dimensional structures are in effect three-dimensional portions of space, two or one of their characteristic scales being very small.

Another fundamental property of fractals, which distinguishes them in a basic manner from homogeneous euclidean objects, is the scaling invariance. Specifically, many fractals are made up of parts which are, in some way, similar to the whole, such as self-similar fractals constructed by iterative procedures shown in Figs. 1–3. Notice that every piece of a self-similar structure holds the key to the whole structure. In other words, if we look at the fractal structure from afar, it appears the same as it does in a close-up view, in terms of its details. The length (area, volume, hyper-volume) scaling of a regular (self-similar) fractal is determined by the unique scaling exponent called the dimension of similarity, D_S (see Table II). Furthermore, for such a structure, all definitions of the metric (Table I) and fractal (Table II) dimensions lead to the same metric dimension number, D, which is equal to the similarity dimension. The latter is determined by the geometric parameters of structure (see Table III and Figs. 1–3).

Natural fractals such as failure patterns possess scaling invariance only in statistical sense: *while the visual images are different in different scales, the roughness and fragmentation neither tend to vanish, nor fluctuate up and down, but remain essentially unchanged as one zooms in continually and examination is refined.* In this way, for random (natural) fractals, the concept of similarity must be replaced by the concept of "statistical self-similarity" and we we can speak about two broad categories, namely the regular (self-similar) fractals, such as shown in Figs. 1–3, and random (statistically self-similar) fractals, such as failure patterns in solids, polymer molecules, coastlines of islands, etcetera. Example of construction of random (statistically self-similar) Koch curve by iteration procedure is shown in Fig. 4b.

[1]However, roughness and fractal dimension are not synonymous. Roughness is generally measured as the average variation about the mean value, and is not related to the scale or changes in scale of measurement. Fractal dimension is used to quantify the variation of the length or area with changes in the scale of measurement interval. Hence the fractal dimension is an intensive property, while roughness is not.

TABLE I. Some different definitions of metric dimension.

NN	Dimension	Measure	Definition of dimension
1	Hausdorff-Besicovitch dimension	$\{U_i\}$ is a δ-cover of F, *i.e.*, $F \subset \bigcup_{i=1}^{\infty}$ with $0 < \lvert U_i\rvert \le \delta$, where U is any non-empty subset of n-dimensional Euclidean space, $\Re^n$. Hausdorff measure is $H^S(F) = \lim_{\delta\to 0} H^S_\delta(F)$, where $H^S_\delta(F) = \inf\Big\{\sum_{i=0}^{\infty} \lvert U_i\rvert^S : \{U_i\}\Big\}$, and diameter of U is $\lvert U\rvert = \sup\{\lvert x-y\rvert : x,y \in U\}$.	$\dim_H F = \inf\{S : H^S(F) = 0\}$ $= \sup\{S : H^S(F) = \infty\}$
2	Mincowski-Bouligand dimension (logarithmic density)	Let $N_\delta(F)$ denotes the least number of balls in a covering of F by balls of radius ε. It is follows from the definition of H^S_δ that $H^S_\delta(F) \le (2\delta)^S \times N_\delta(F)$.	$\Delta(F) = \overline{\lim}_{\delta\to 0}\{\lg N_\delta(F)/\lg(1/\delta)\}$, $\Delta(F) \ge \dim_H F$
3	Divider dimension (of Jordan curves)	$M_\delta(C)$-maximum number of points $x_0, x_1, \ldots, x_m$, on the curve C, in that order, such that $\lvert x_k - x_{k-1}\rvert = \delta$, $k = 1, 2, \ldots, m$.	$D_D = \lim_{\delta\to 0}\{\lg M_\delta(C)/\lg(1/\delta)\}$
4	Packing dimension	$\{B_i\}$ is a collection of disjoint balls of radius at most δ with centers in F. Packing measure is $P^S(F) = \inf\Big\{\sum_i P^S_0(F_i) : F \subset \bigcup_{i=1}^{\infty} F_i\Big\}$, where $P^S_0 = \lim_{\delta\to 0} P^S_\delta(F)$, $P^S_\delta = \sup\{\lvert B_i\rvert^S : \{B_i\}\}$.	$\dim_P F = \inf\{S : P^S(F) = 0\}$ $= \sup\{S : P^S(F) = \infty\}$, $\dim_H F \le \dim_P F \le \Delta(F)$

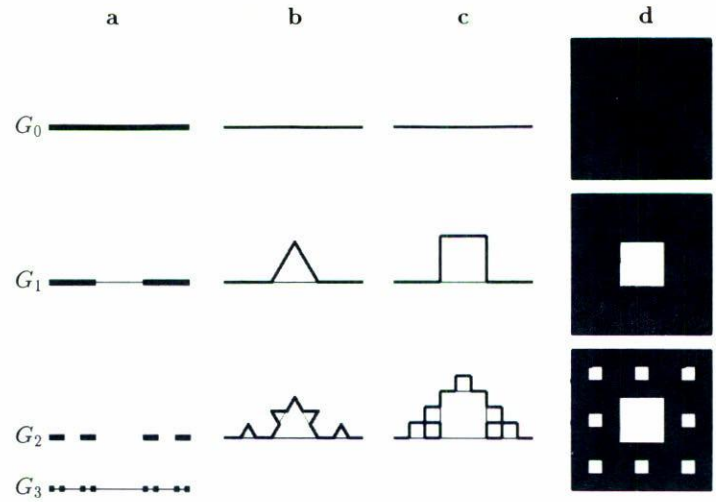

FIGURE 1. Two first stages of the classical construction of regular (self-similar) fractals by iteration procedure. The fractal geometry is obtained for an infinite number of iterations, *i.e.* $F = G_{n=\infty}$, where G_n is the pre-fractal of order n. The metric dimension (see Table I) of F is equal to its similarity dimension (see Table II) and can be calculated by using the corresponding relationship from Table III. The Cantor set of points (a) has the topological dimension $d = 0$ and the fractal dimension $D_S = \ln 2/\ln 3 = 0.63\ldots$; the triadic Koch curve (b) has $d = 1$ and $D_S = \ln 4/\ln 3 = 1.26\ldots$; the Koch curve (c) has $d = 1$ and $D_S = \ln 5/\ln 3 = 1.46\ldots$; and the Sierpinski carpet has $d = 1$ and $D_S = \ln 8/\ln 3 = 1.89\ldots$. Note, that the baseline cross-sections of these fractals have the same fractal dimension $D_S = \ln 2/\ln 3$.

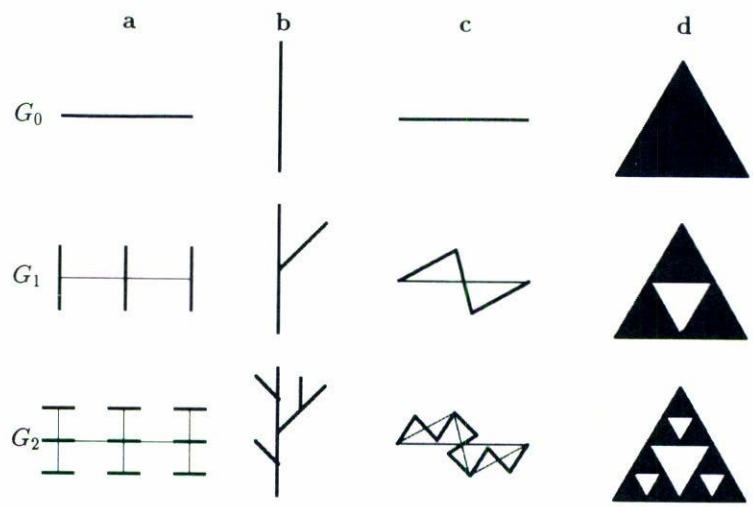

FIGURE 2. Two first stages of the construction of the "Cantor-like" set of points (a), "tree-like" fractal (b), "Koch-like" curve (c), and Sierpinski gasket (d). Notice that all these fractals have the same fractal dimension $D_S = \ln 3/\ln 2 = 1.584\,962\,501\ldots$, whereas theirs connectivity property are different. Moreover, the topological dimension of the "Cantor like set of point" is zero, whereas fractals (b), (c), and (d) have the topological $d = 1$.

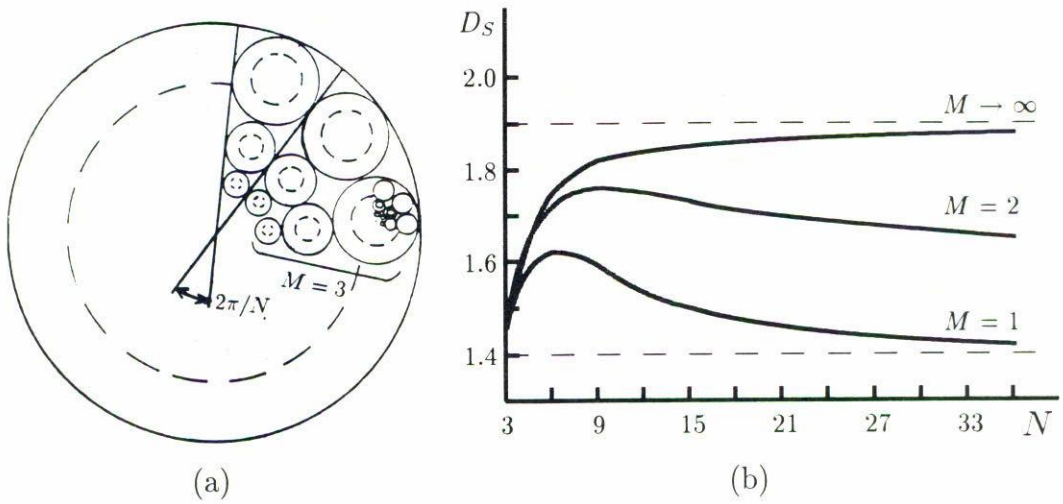

FIGURE 3. The circle fractal (a) and corresponding dependence D_S on the structure parameters N and M (b) calculated by means equation system from Table III (b).

TABLE II. Some definitions of fractal dimension.

NN	Dimension	Expression for Fractal dimension	Comments
1	Mandelbrot, Schirelman-Kolmogorov	$D_F = \lim_{\varepsilon\to 0}\{\sup[\ln N_x(\varepsilon)/\ln(1/\varepsilon)]\}$ $= \inf\left\{d \geq 0, \quad \lim_{\varepsilon\to 0}\left[\sup \varepsilon^d \times N_x(\varepsilon) = 0\right]\right\}$	$N_x(\varepsilon)$ is the least number of balls of radius less than ε which are needed to cover fractal
2	Kolmogorov, Schirelman-Potjrajin	$D_K = \lim_{\varepsilon\to 0}\{\sup \lg N(\varepsilon)/\lg(1/\varepsilon)\}$	$N(\varepsilon)$ is the smallest number of balls of diameter less or equal to ε which are needed to cover fractal
3	Similarity	$D_S = \ln M/\ln R$	If set made up of M copies of itself scaled by factor R
4	Internal similarity	$\sum_{i=1}^{d} R_i^{d_{IS}} = 1$	d: topological dimension, R_i: similarity ratios
5	Cluster (or mass) dimension	$D_M = \ln N/\ln(R/R_0)$	N is the number of monomers of length R_0 into monomers of dimension R

TABLE III. Relations between similarity dimension and parameters of structure for different regular fractal structures.

NN	Type of regular fractal structure	Expression for Fractal dimension	Comments
1	Cantor set, Peano curves, Koch curves	$D_S = \dfrac{\ln N}{\ln(1/\varepsilon)}$	N: number of self-similar parts, ε: concern length of each part (Figs. 1a–1c and 2a–2c)
2	"Firtrees"	$D_S = \dfrac{\ln P}{\ln K}$	P: number of branch with length L_{n+1} on the branch with length L_n. $K = L_n/L_{n+1}$ (Fig. 2b)
3	Sierpinski gaskets (carpets)	$D_S = \dfrac{\ln(b^d - R)}{\ln b}$	b: the base of lattice, R: number of ejection parts, d: topological dimension (Figs. 1d and 2d)
4	Round fractal lattice	$N\varphi^{D_S}\sum_{k=1}^{M}(1-2\varphi)^{D_s(k-1)} = 1,$ $\varphi = \tan(\pi/N)\tan[(\pi/4)(1-2/N)]$	N: number of sectors, M: number of possible scale transformations (Fig. 3)

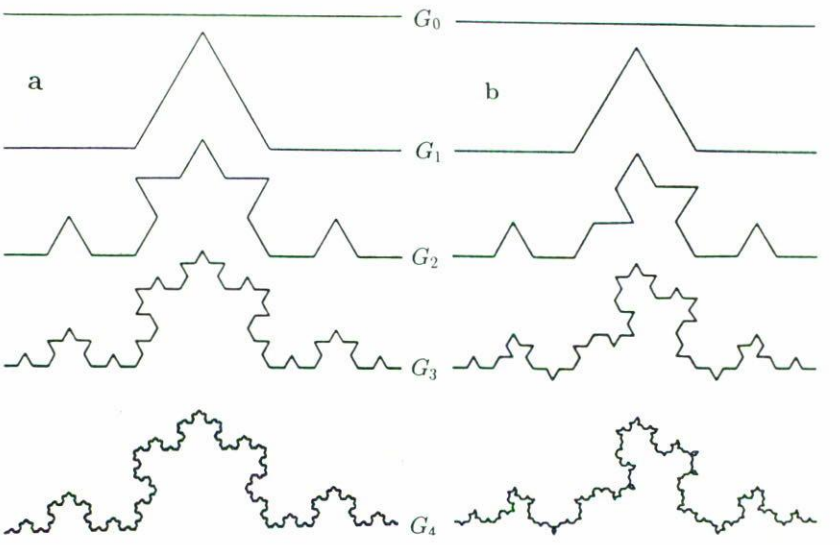

FIGURE 4. Self-similar (a) and statistically self-similar (b) versions of the triadic Koch curve (see also Fig. 1b). Notice that these curves are homeomorphic and characterized by the same metric dimension $D = \ln 4/\ln 3 = D_S$ [52].

TABLE IV. The properties which must be hold for any reasonable definition of dimension.

NN	Property	Relation for dimension	Conditions
1	Monotonicity	$\dim_H E \leq \dim_H F$	If $E \subset F$
2	Stability	$\dim_H F = \max\{\dim_H E, \dim_H A\}$	If $F : E \cup A$
3	Countable stability	$\dim_H\left\{\bigcup_{i=1}^{\infty} F_i\right\} = \sup_{1\leq i\leq\infty}\{\dim_H F_i\}$	If F_i is a (countable) sequence of sets
4	Geometric invariance	$\dim_H f(F) = \dim_H F$	If $f(F)$ is a transformation of $\Re^n$ such as a translation, rotation, similarity, affinitty
5	Lipschitz invariance	$\dim_H f(F) = \dim_H F$	If $f(F)$ is bi-Lipschitz transformation, *i.e.* $C_1 \cdot \lvert x-y\rvert \leq \lvert f(x)-f(y)\rvert \leq C_2 \cdot \lvert x-y\rvert$, for $(x, y \in F)$ and $0 < C_1 \leq C_2 < \infty$

It is easy to see that all definitions of the metric (fractal) dimension given in Tables I and II satisfy some fundamental properties listed in the Table IV (obviously, any reasonable definition of the dimension number should satisfy these properties). Therefore, *any random but statistically self-similar fractal can be transformed in the regular (self-similar) fractal with the same metric (fractal) dimension by means of a homeomorphic, one-to-one and onto transformation.* Hence, for a statistically self-similar fractals all definitions of metric dimension listed in Table I are also equivalent and lead to the same dimension number, which is equal to the similarity dimension of the homeomorphic regular fractal. For example, two curves in Fig. 4 are characterized by the same value of metric dimension, $D = D_S = \ln 4/\ln 3$. In this way, natural statistically self-similar fractal patterns can be advantageously modeled by the corresponding regular fractals with the same fractal dimension[2] as, for example, it is shown in Fig. 5.

Clearly the knowledge of the fractal dimension does not tell everything about the morphology of the system. For example, two systems with the same fractal dimension may actually look very different and have very different connectivity properties. For example, all fractals in Fig. 2 have the same fractal dimension $D_S = \ln 3/\ln 2$, whereas the images and connectivity properties of these fractals are different. Moreover, the topological dimension of the "Cantor like set of points" (Fig. 2a) is zero, while the topological dimension of tree-like fractal (Fig. 2b), Koch curve (Fig. 2c) and Sierpinski gasket (Fig. 2d) is one.

[2]For isotropic (statistically) self-similar patterns almost any reasonable procedure for measuring the fractal dimension will lead to essentially the same results if the fractal scaling regime extends over a sufficiently wide range of length scales.

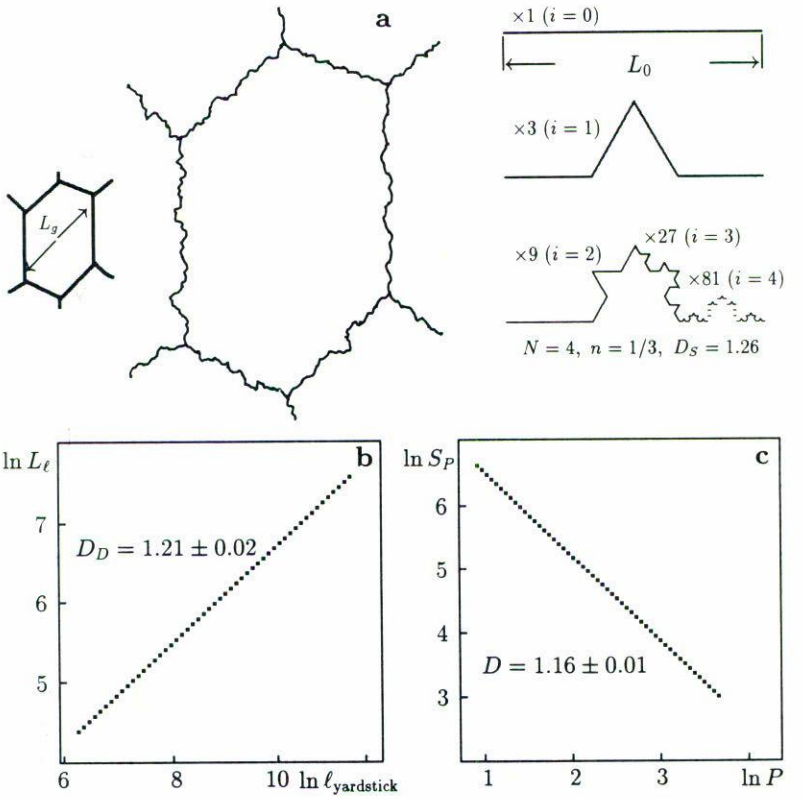

FIGURE 5. The grain boundary approximation by regular fractal curve (a); and the results of experimental evaluation of the fractal dimension D of grain boundaries in deformed zinc [3]: (b) by means of the yardstick (divider) method, and (c) by using the perimeter-area relation for the grain ensemble.

Furthermore, statistically self-similar fractal patterns are essentially isotropic, whereas real fracture surfaces in solids often have anisotropic asperity distributions. For a description of such patterns the concept of self-similarity has been extended to account for anisotropy through the notion of self-affinity. The fundamental difference between self-similar and self-affine fractals is the way in that scaling will produce statistical equivalence. Self-similar fractals may be scaled equally in the all directions to produce statistically equivalent profiles, whereas self-affine fractals must be scaled by different amounts in the different directions to produce statistical equivalence. A self-affine pattern is statistically invariant under an affine transformation

$$x' \to \lambda_x x, \qquad y' \to \lambda_y y, \qquad z' \to \lambda_z z. \tag{1}$$

Requiring that such transformations be combined, a group structure is implied. As a consequence λ_y and λ_z have to be homogeneous functions of, say, λ_x; both scale as

$$\lambda_y \propto \lambda_x^{\nu_y}, \qquad \lambda_z \propto \lambda_x^{\nu_z}, \tag{2}$$

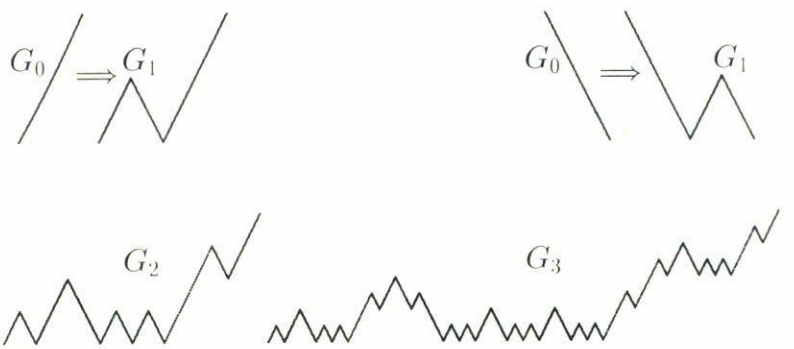

FIGURE 6. Invariant construction of self-affine fractal by means of affine transformations [55]. The self-affine curve $Z(X)$ with $H = 0.5$ is obtained after infinite number of iterations.

but the exponents ν_y and ν_z are in general different. If so, then $\lambda_z \propto \lambda_y^H$, where the roughness exponent H, also called the Hurst exponent, is given by the relationship

$$H = \frac{\nu_z}{\nu_y}. \tag{3}$$

In the special case of an isotropic self-affine surface with mean plane parallel to the coordinate plane (x, y), we have $\nu_y = 1$, so that $H = \nu_z$ the last relation is also valid for any self-affine curve on a two-dimensional plane (see Fig. 6). However, generally the self-affine scaling must be characterized by $d - 1$ scaling exponents in d-dimensional Euclidean space. Specifically, a rough fracture surface is generally characterized by two scaling exponents.

In the application of fractal models to real fracture surfaces the concepts of self-affinity and self-similarity must be carefully distinguished even in the case of isotropic surface, because of the vertical cuts of such a surface (which are commonly studied in fractographic investigations [3]) are statistically self-affine, whereas horizontal cuts (which are used in the popular slit-island method of the fractal dimension measurement [8]) are statistically self-similar. Because of this, different studies dealing with fractal characterization of fracture surfaces have given inconsistent results, raising questions about the comparison of various works and their interpretation. The difference in the scaling properties of vertical and horizontal cuts must be taken in mind when the results of different investigations are discussed. Below, this aspect of fractal measurements will be discussed in more details.

2.1. MODEL REPRESENTATIONS OF FRACTURE SURFACES

It is now clearly established that fracture surfaces as well as their profiles can be treated as self-affine objects and in this way they may be advantageously modeled by using the fractal (self-affine) functions [7]. Despite the non-differentiability of fractal functions, now it is beyond the question that the fractal representation of failure patterns can hardly benefit our understanding the nature and mechanisms of failure phenomena [10–45]. The fractal models of crack faces have at least two remarkable features. First, they are locally invariant with respect to a scaling transformation. Secondly, the fractal function

is an essentially multiscale. Therefore, it allows one to model a real fracture surface with multiscale roughness, including the existence of characteristic scales which are both much greater and less than the incident wavelength. Experimental investigations studies using various experimental techniques (profilometry, microscopy and image analysis, scanning tunneling electron microscopy, electrochemistry, etc.) on materials as different as steels, metal alloys, rocks, polymers, and ceramics, have shown that fracture surfaces exhibit scaling properties on two or three decades of length scales (see Refs. 3–7 and references therein).

An ideal self-affine profiles may be modeled using the simple algorithm suggested by Voss [55]. For (1 + 1)-dimensional profiles the basic procedure is as follows: knowing the values of z at both i and j of a root segment, we compute its value at the center k as the average $(z_i + z_j)/2$ plus a fluctuation $æ\delta z$. At each generation n, the fluctuation δz_n is picked from a statistical distribution $F(\delta z)$ with zero mean and scaled by a factor æ proportional to the length of the parent segment $|i - j|$ raised to the power H. The distribution F can be chosen, without any loss of generality, to be a Gaussian distribution.

In this way, a rough surface is defined by a vertical height profile above a horizontal (x, y) plane, an may be represented by a single-valued random function $z(\mathbf{r})$ of the in-plane horizontal vector $\mathbf{r} = (x, y)$. Figures 7a and 7b show examples of profiles constructed in such a manner using two different exponents $H = 0.49$ and $H = 0.85$, respectively. These profiles possess self-affine scaling (2). To show this, let us define the smallest length scale or unit length scale $l_0 = 1$ and measure by this scale the curve length $L_{AB} = N \times l_0 = N$ between two arbitrary points A and B on the profile. This is equivalent to regarding the curve as consisting of particles of diameter l_0 and counting the number of particles between points A and B. We then calculate x- and z-variance $\langle X^2 \rangle$ and $\langle Z^2 \rangle$ of all measured points on the profile between the two points A and B:

$$\langle X^2 \rangle = \frac{1}{N} \sum_{i=1}^{N} (x_i - x_c)^2 , \qquad \langle Z^2 \rangle = \frac{1}{N} \sum_{i=1}^{N} (z_i - z_c)^2 , \tag{4}$$

with

$$x_c = \frac{1}{N} \sum_{i=1}^{N} x_i , \qquad z_c = \frac{1}{N} \sum_{i=1}^{N} z_i ,$$

where (x_i, z_i) is the coordinate of the i-th measured point on the profile. The standard derivations $\langle\langle X \rangle\rangle = \sqrt{\langle X^2 \rangle}$ and $\langle\langle Z \rangle\rangle = \sqrt{\langle Z^2 \rangle}$ indicate the approximate sizes of the part of the profile. Repeat the measurement procedures described above for many pairs of points on the curve and check by the log-log plots of $\langle\langle X \rangle\rangle$ and $\langle\langle Z \rangle\rangle$ versus N whether they possess the self-affine scaling (2) in the form

$$\langle\langle X \rangle\rangle \propto N^{\nu_x} , \qquad \langle\langle Z \rangle\rangle \propto N^{\nu_z} . \tag{5}$$

If so, they are then related to each other as

$$\langle\langle Z \rangle\rangle \sim \langle\langle X \rangle\rangle^H , \tag{6}$$

where the Hurst exponent is given by relation (3).

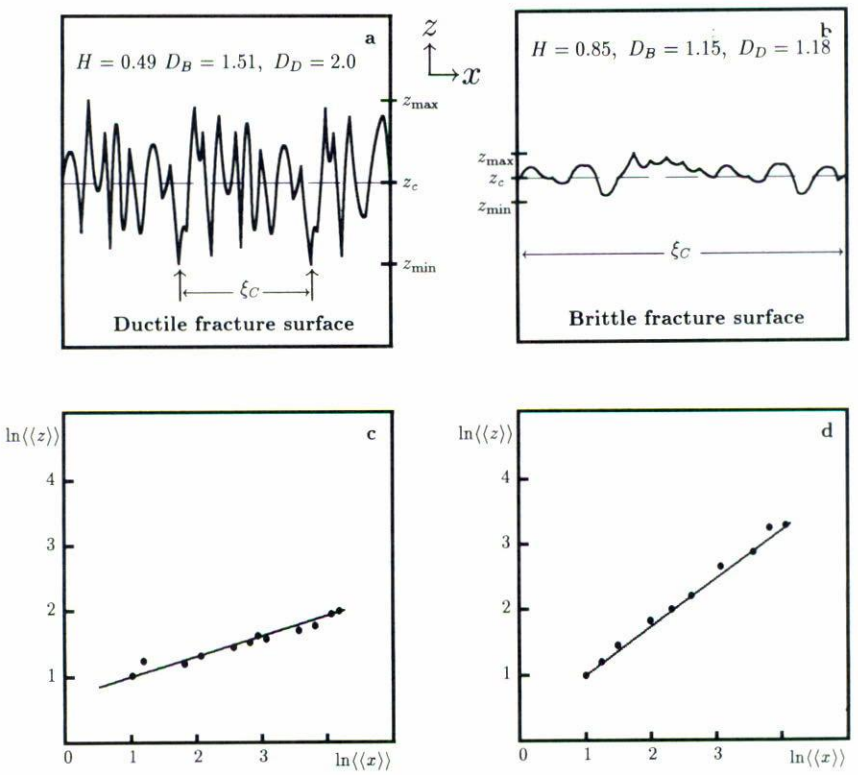

FIGURE 7. The self-affine image of a ductile (a) and brittle (b) fracture surfaces constructed by the Voss's algorithm described in text and the corresponding plots for standard derivation Z versus standard derivation X in log-log coordinates. Solid lines represent theoretical behavior (6) with $H = 0.49$ (c) and $H = 0.85$ (d); points—results of computations.

As Figs. 7c and 7d suggests, the profiles in Figs. 7a and 7b obey power law scaling (6) and so they are possess self-affine geometry and in this way they can me used as model representations for vertical cuts of brittle and ductile fracture surfaces [4, 10].

Another notable example of a single-valued self-affine curve in plane is the graph of the single-valued continuous, but nowhere differentiable Mandelbrot-Weierstrass function [56]

$$z(x) = \sum_{k=0}^{\infty} \lambda^{-kH} \left[1 - \exp\left(i\lambda^k x\right)\right] \times \exp\left(i\alpha_k\right), \tag{7}$$

where $\lambda > 1$, $0 < H < 1$ and the phases α_k are arbitrary (α_k may be chosen by a special rule or may be considered as independent random variables uniformly distributed between 0 and 2π). The graphs $\mathrm{Re}\, z(x)$ and $\mathrm{Im}\, z(x)$ possess self-affine scaling (2). This implies that the whole function $z(x)$ can be reconstructed from its values in the range $x_o \le x < \lambda x_o$; for example, $z(x)$ in the ranges $\lambda x_o \le x < \lambda^2 x_o$ and $\lambda^{-1} x_o \le x < x_o$ are magnified and diminished versions, respectively, of $z(x)$ in the range $x_o \le x < \lambda x_o$. Notice that the graph of (7) is statistically equivalent (see Ref. 57) to the profile constructed by considered above algorithm when the corresponding Hurst exponents are equal.

The non-differentiability property of the fractal function (7) can be formally expressed in terms of the Hölder inequality

$$\lim_{\Delta x \to 0} [z(x + \Delta x) - z(x)] \leq C (\Delta x)^H , \tag{8}$$

where C is a constant and $0 \leq H < 1$.

The univariable function (7) can be easily generalized to two variables to model self-affine surfaces. Specifically, an isotropic in a mean plane self-affine fracture surface may be usefully represented by the function

$$z(\mathbf{r}) = \sum_{k=-\infty}^{\infty} \lambda^{-Hk} \left[1 - \exp\left(i\lambda^k |\mathbf{r}|\right)\right] \times \exp(i\alpha_k) , \tag{9}$$

where $|\mathbf{r}| = |\sqrt{x^2 + y^2}|$, $\lambda > 1$ and $0 < H < 1$. Notice that the vertical cuts of the graphs of $\operatorname{Re} z(\mathbf{r})$ and $\operatorname{Im} z(\mathbf{r})$ are statistically self-affine, with H defined by Eq. (3), whereas the horizontal cuts of the same graphs are statistically self-similar fractals for which the Hurst exponent defined by Eq. (3) equals one. Hence the Hurst exponent is useless when discussing both self-affine and self-similar fractals in the same context!

An anisotropic fracture surface may be modeled by the following two-variable function of the Mandelbrot-Weierstrass type:

$$\begin{aligned} z(\mathbf{r}) &= \sum_{k=-\infty}^{\infty} \left(æ\lambda^k\right)^{-H} \{1 - \exp[iæ\lambda^n(ax + by)]\} \times \exp(ik\alpha_k) \\ &= \sum_{k=-\infty}^{\infty} \left(æ\lambda^k\right)^{-H} \left\{1 - \exp\left[iæ\lambda^n(a^2 + b^2) r \cos(\beta - \gamma)\right]\right\} \times \exp(iæ\alpha_k) , \end{aligned} \tag{10}$$

where $\beta = \arctan(y/x)$, $\gamma = \arctan(b/a)$ and æ is a constant.

All these functions possess the following statistical properties

$$\langle Z(\mathbf{r}) - Z(\mathbf{r} + \Delta\mathbf{r}) \rangle = 0, \qquad \langle |Z(\mathbf{r}) - Z(\mathbf{r} + \Delta\mathbf{r})|^2 \rangle \sim (\Delta\mathbf{r})^{2H} ,$$

$$\langle Z(\mathbf{r}) Z(\mathbf{r} + \Delta\mathbf{r}) \rangle \sim (\Delta\mathbf{r})^{2H} , \tag{11}$$

where $Z(\mathbf{r}) = \operatorname{Re} z(\mathbf{r})$, and they are characterized by a spatial spectrum $W(q)$ of a power law type

$$W(q) = C|\mathbf{q}|^{-(1+2H)}, \tag{12}$$

which has been observed in experiments on X-ray scattering from the fracture surfaces in solids [58] and in experiments on light scattering from the surface of the moon [59].

Now, if we define the correlation function as [58]

$$C(\mathbf{r}) = \frac{\langle -Z(-\mathbf{r})\, Z(\mathbf{r}) \rangle}{\langle Z^2(\mathbf{r}) \rangle}, \tag{13}$$

then using Eqs. (7) and (9)–(11) it is easy to show that $C(r)$ does not depend on r (see also Refs. 56, 58) and it is equal to

$$C(r) = 2\left(2^{2H-1} - 1\right) = C^*. \tag{14}$$

The sign of C^* determines the type of correlations of the functions (7), (9), and (10), which is determined by the value of H. Namely, if $H > \frac{1}{2}$ then $C^* > 0$ and the functions (7), (9), and (10) display persistence, *i.e.*, a trend (for example, a high or low value) at r is likely to be followed by a similar trend at $r + \Delta r$, whereas if $H < \frac{1}{2}$, then $C^* < 0$ and functions generates antipersistence, *i.e.*, a trend at r is not likely to be followed by a similar trend at $r + \Delta r$. For $H = \frac{1}{2}$ the graphs of functions (7), (9), and (10) represent the trajectories of a random walk for which $C^* \equiv 0$ [58].

In Refs. 10, 12 and 42 have been suggested that the ductile cracks are characterized by antipersistence behavior whereas the brittle cracks possesses persistence behavior. This leads to difference in statistical properties of brittle and ductile fracture surfaces the images of which are shown in Figs. 7a and 7b.

Notice that a self-similar function cannot display antipersistence, since for any D the correlation integral (13) is equal to

$$C(x) = C^* = 2^{2(d-1)/D-1} - 1 \geq 0,$$

i.e., only brittle fracture surfaces can be modeled by homeomorphic self-similar fractals, whereas ductile fracture patterns should be always treated as statistically self-affine fractals.

In Refs. 10 and 12 was shown that the stress behavior in the vicinity of crack tip is governed by the roughness exponent H and does not depend on the actual geometry of crack faces. Therefore, in the problem with self-affine crack, a complex geometry of real crack face can be modeled by homeomorphic deterministic pattern which is statistically equivalent to the actual crack pattern. This representation is very useful for theoretical analysis to the problem.

2.2. FRACTAL CHARACTERIZATION OF SELF-AFFINE FRACTURE SURFACES

The constructions and procedures that fractal geometry has borrowed from mathematics all involved infinite interpolation. In Nature, on the other hand, interpolations cannot proceed without end, and constructions tend to proceed by extrapolation. In the self-similar case the infinitesimal techniques extend via power law relationships valid uniformly at all scales, whereas in the self-affine case, the two basic procedures involve different tools.

One of the most often used methods to characterize the fractal properties of an object is to estimate its fractal dimension. Although it seems natural to associate the fractal dimension with a pattern that fulfills some kind of scale invariance, it has been recognized for a long time that the very concept of fractal dimension is not well defined as soon as the symmetry obeyed by the pattern is not a pure self-similarity. The reason for such a statement is that the fractal dimension gives the scaling of a measure within a length scale. For a self-affine object, the scaling with the distance along one axis

TABLE V. Relationships between roughness (Hurst) exponent and various fractal dimensions for self-similar and self-affine fractals with topological dimension equal to $d-1$ embedded in d-dimensional Euclidean space.

Dimension	Self-affine fractals		Self-similar fractals
	Local limit	Global limit	
Similarity, D_S	—	—	$(d-1)/H$
Hausdorff-Besicovitch, D_H	$d-H$	$d-1$	$(d-1)/H$
Box-counting, D_B	$d-H$	$d-1$	$(d-1)/H$
Divider, D_D (compass, rule)	Latent fractal dimension: $D_\ell = \begin{cases} (d-1)/H, & \text{if } H > (d-1)/d; \\ d, & \text{if } H \le (d-1)/d. \end{cases}$	$d-1$	$(d-1)/H$
Contour ($d=2$), D_{cn} (single coastline)	$2/(1+H)^*$ $1+(1-H)/(\nu+1)^\dagger$	$d-1$	$1/H$
Gap,‡ D_G	$\dfrac{\lg N}{\lg b^+}$	—	$(d-1)/H$
Mass,§ D_M	$\log_{b'}\left(\dfrac{Nb''}{b'}\right)$	$\log_{b''}\left(\dfrac{Nb'}{b''}\right)$	$(d-1)/H$

* Mean field approximation.

† ν is the correlation length exponent from percolation theory.

‡ N is the number of similar parts, $b^+ = (r_1 r_2 \dots r_d)^{1/d}$ is the effective base, r_i is the concern length of each part in i-direction (for self-similar fractal all r_i equals to r).

§ $b' = \max r_i$ and $b'' = \min r_i$ are the largest and smallest base of self-affine transformation (for self-similar transformation $b' \equiv b''$).

may differ depending on the orientation of the axis. Because of this, the roughness exponent H is the more adequate characteristics for self-affine scaling. However, in actual practice of fractographic investigations the fractal dimension of the vertical or horizontal cuts of the fracture surface is more commonly measured [1–3]. The vague definition of fractal dimension for a self-affine object has, in the past, resulted in some misuse of the fractal dimension in this framework, as well as some confusions in the measure of this property. Specifically, these confusions lead to aforementioned contradictions between results obtained by different experimental techniques (see, for example, discussion in Refs. 33, 34, 50, 51, 60–63 and references therein).

Actually, in the contrast to self-similar fractals the fractal dimension of an anisotropic self-affine pattern is not uniquely defined. First of all we must distinguish between the

TABLE VI. Some definition of box-counting (or box) dimensions.

Dimension	Definition	Comments
Lower box-counting (or lower-box)	$\underline{\dim}_B F = \underline{\lim}_{\delta\to 0}\left\{\dfrac{\log N_\delta(F)}{\log \delta}\right\}$	F is non-empty subset of $\Re^n$. $N_\delta(F)$ is any of the following: A. The smallest number of 1) closed balls of radius δ 2) cubes of side δ 3) sets of diameter at most δ, that cover F B. The largest number of disjoint balls of radius δ with center in F C. The number of δ-mesh cubes that interset of F.
Upper box-counting (or upper-box)	$\overline{\dim}_B F = \overline{\lim}_{\delta\to 0}\left\{\dfrac{\log N_\delta(F)}{\log \delta}\right\}$	
Box-counting (or box)	$\dim_B F = \lim\limits_{\delta\to 0}\left\{\dfrac{\log N_\delta(F)}{\log \delta}\right\}$	
Minkowski	$\dim_B^M(F) = n - \lim\limits_{\delta\to 0}\left\{\dfrac{\log \mathrm{vol}^n(F_\delta)}{\log \delta}\right\}$	F_δ is the δ-parallel body to F: $F_\delta = \{x \in \Re^n : \lvert x-y\rvert \le \delta,$ for some $y \in F\}$ where n is the topological dimension.
Lower modified box-counting	$\underline{\dim}_{MB} F = \inf\left\{\sup\limits_i \underline{\dim}_B F_i : F \subset \bigcup\limits_{i=1}^{\infty} F_i\right\}$	If F can be decomposed into a countable number of pieces F_i in such a way that the largest piece has a small a dimension as possible.
Upper modified box-counting	$\overline{\dim}_{MB} F = \inf\left\{\sup\limits_i \overline{\dim}_B F_i : F \subset \bigcup\limits_{i=1}^{\infty} F_i\right\}$	
$\dim_H F \le \underline{\dim}_B F \le \overline{\dim}_B F$ $0 \le \dim_H F \le \underline{\dim}_{MB} \le \overline{\dim}_{MB} F = \dim_P F \le \overline{\dim}_B F \le n$		

local ($\Delta L \ll \xi_C$) and global ($\Delta L \gg \xi_C$) fractal dimensions [38, 44], where ΔL is the characteristic scale of measurements and ξ_C is the self-affine correlation length.[3] The global fractal dimension always equals the topological dimension of self-affine pattern, while in the local limit different definitions for fractal dimension lead to different dimension numbers which are associated with different scaling properties of a self-affine fractal [4]. The relationships between the Hurst and some different fractal dimensions are given in Table V. Notice that different fractal dimensions associate with different experimental techniques (see Tables I, and VI, VII).

[3]The existence of a well defined correlation length ζ_C [68] is the distinctive feature of a self-affine fractal, which distinguishes them from (statistically) self-similar patterns, the fractal properties of which are limited only by physical factors [3, 64].

TABLE VII. Definitions of some other fractional dimensions

Dimension	Definition	Comments
Capacity dimension	$\dim_C F = \begin{cases} 0, & \text{if } C_\alpha(F) = 0,\ \forall\, \alpha > 0; \\ d_C > 0, & \text{if } C_\alpha(F) = 0,\ \forall\, \alpha > d_C; \\ & \text{and } C_\alpha > 0,\ \forall\, 0 < \alpha < d_C. \end{cases}$	Capacity is $C_\alpha = \begin{cases} [W_\alpha(F)]^{1/\alpha}, & \text{if } W(E) < \infty; \\ 0, & \text{otherwise;} \end{cases}$ where $W_\alpha(F) = \inf\{I_{\alpha,m}(F)\}$, $I_{\alpha,m} = \iint_F \|x - y\|^{\alpha - n}\, dm(x)\, dm(y)$, for each $0 < \alpha < n$, where n is a topological dimension F and $\|\ldots\|$ is the euclidean norm.
One-sided dimension (of boundary F of set A in $\Re^n$)	$\dim_{OS} F = n - \lim_{\delta \to 0} \left\{ \dfrac{\log \mathrm{vol}^n(F \cap A)}{\log \delta} \right\}$	F is the boundary of a set A; F_δ is the δ-parallel body of F: $F_\delta = \{x \in \Re^n : \lvert x - y \rvert \le \delta, \quad \text{for some } y \in F\}$, where n is a topological dimension.
Fourier dimension	$\dim_F = \max\left\{ t : \lvert\hat{\mu}(U)\rvert \le B\lvert U\rvert^{-t/2} \right\}$, for some constant B, where the mass distribution $\hat{\mu}(U)$ on $\Re^n$ is $\hat{\mu}(U) = \int_{\Re^n} \exp(ix \cdot U)\, d\mu$, where $U \in \Re^n$ and $x \cdot U$ represents usual scalar product.	If $\lvert\hat{\mu}(U)\rvert \le B\lvert U\rvert^{-t/2}$ for some constant B, $\hat{\mu}(U)\rvert \le \mu(\Re^n)$ for all U, we have $I_k(\mu) = (2\pi)^n C \int \lvert U\rvert^{k-n} \lvert\hat{\mu}(U)\rvert^2\, dU$ $\le C_1 \int_{\lvert U\rvert \le 1} \lvert U\rvert^{k-n}\, dU + C_2 \int_{\lvert U\rvert\, 1} \lvert U\rvert^{k-n} \lvert U\rvert^{-1}\, dU$ which converges if $k < t$.

TABLE VII. (Continued).

Dimension	Definition	Comments
Menger-Urysohn	The $\dim_{(M-U)} F$ is defined inductively as follows: 1) The empty set F has $$\dim_{(M-U)} F = -1,$$ 2) A topological space F has $$\dim_{(M-U)} F = n,$$ if n is the largest natural number such that each point of F has arbitrarily small neighborhoods with frontiers of dimension less than n.	A. If every point p of space F has arbitrarily small neighborhoods with empty frontier (*i.e.*, for every neighborhood U of p there exist a neighborhood V of p that $V \subset U$, $\mathrm{fr}\,(V) = \emptyset$) then $\dim_{(M-U)} F = 0$. B. The set of irrational numbers, the Cantor set and any countable space are of dimension 0 is itself zero dimensional. C. If X is a separable metric space, then $$\dim_{(M-U)} X = \inf\{\dim_H X'\},$$ where the minimum is taken over the set of spaces X' homotropic to X. D. If $\dim_{(M-U)} X - \dim_{(M-U)} Y = K > 0$, then there exist point of Y whose inverse image under F has $\dim_{(M-U)} \geq K$.
Dimension print	Print$F$ of subset F is defined to be the set of non-negative pairs (k, p) for which $$H^{k,p}(F) > 0.$$	U is a rectangle (the sides need not be parallel to the coordinate axes). Let $a(U) \geq b(U)$ is the length of sides of U; k and p are non-negative numbers. For F a subset of $\Re^2$, $$H^{k,p} = \lim_{\delta \to 0} H_\delta^{k,p}(F),$$ $$H_\delta^{k,p}(F) = \inf\Big\{\sum_i a(U_i)^k\, b(U_i)^p : \{U_i\} \text{ is a } \delta\text{-cover of } F \text{ by rectangles}\Big\}.$$ Here, $H^{k,0}$ is just the k-dimensional Hausdorff measure.

Furthermore, for a real fracture surface self-affine scaling regime is bounded by upper and lower correlation lengths ξ_i and ℓ_0 in both the horizontal (r) and vertical (z) directions, *i.e.*, self-affine scaling is found over the range

$$\ell_0 < \Delta r < \xi_r, \qquad \ell_0 < \Delta z < \xi_z, \tag{15}$$

and these correlation lengths are related by

$$\frac{\xi_z}{\ell_0} = \left(\frac{\xi_r}{\ell_0}\right)^H. \tag{16}$$

So that a real fracture surface obeys scaling properties (2), (11), (12), and (14) only within the length scale interval

$$\ell_0 < L_x < \xi_C = \sqrt{\xi_r \xi_z}\,, \tag{17}$$

where L_x is the length of crack projection on the direction of crack propagation, and ℓ_0 is the microscopic cutoff determined by the actual failure processes in nanoscale [6, 7]. The experimental data indicate that for brittle fracture surfaces ℓ_0 is of the order of $10^{-8} \div 10^{-6}$ m and $\xi_C \sim 10^{-3} \div 10^{-2}$ m [3]. Furthermore, the fracture surface roughness exponent H in the case of brittle fracture is more than a certain critical value H_c, whereas a ductile fracture surface is characterized by $H < H_c$ [12, 42]. Hence an accurate estimation of the self-affine exponent may have deep physical implications and is of crucial importance for the identification the nature and mechanisms of fracture. The critical values of H and related critical values of different fractal dimensions are given in Table VII for two classical problems in fracture mechanics.

According to Eqs. (11), in the limit $\Delta\mathbf{r} \to \infty$ we have $\langle |Z(\mathbf{r}) - Z(\mathbf{r} + \Delta\mathbf{r})|^2 \rangle \to \infty$, while

$$\frac{\langle |Z(\mathbf{r}) - Z(\mathbf{r} + \Delta\mathbf{r})|^2 \rangle}{|\Delta\mathbf{r}|^2} \to 0, \tag{18}$$

i.e., the model surfaces (9) and (10) are asymptotically flat and so, it is characterized by the integer global fractal dimension. Asymptotically flat surface is a rather ideal case since on real fracture surfaces $\langle |Z(\mathbf{r}) - Z(\mathbf{r} + \Delta\mathbf{r})|^2 \rangle$ at large length scales may saturate to the value $2\sigma^2$, where the parameter $\sigma = \sqrt{\langle |z(\mathbf{0})|^2 \rangle}$ is the RMS-saturated surface roughness [58]:

$$\langle |Z(\mathbf{r}) - Z(\mathbf{r} + \Delta\mathbf{r})|^2 \rangle = 2\sigma^2 \tag{19}$$

for $|\Delta\mathbf{r}| \gg \xi_C$.

Based on their data, authors [34] conjectured that the crack faces roughness exponent H has the universal value close to 0.7. Authors [65] conjectured another universal value $H = 0.8$, the same for brittle and ductile fracture surface. More recently, the authors [46]. conjectured the existence of two universal roughness exponents, namely $H_1 \simeq 0.84$ and $H_2 \simeq 0.45$. However, a certain number of experimental data does not agree with the conjecture of universality for the fracture surface scaling exponent (see, for

example [3, 33, 63] and references therein). Furthermore, various theoretical models and computer simulations also lead to the nonuniversal fractal dimension of crack faces, which usually depends from the variable parameters of the model being used [67, 68]. Finally, there are strong indications that H depends on material properties and mechanisms of fracture when experimental data obtained by the same technique (see, for review, Ref. 3). These observations casts doubt on the hypothesis of universality for fracture roughness exponent.

2.3. MULTIAFFINITY OF REAL FRACTURE SURFACES

Looking at the crack morphology formation problem, one realized that the self-affine geometry of crack faces results from the stochastic nature of crack growth. This issue can be illustrated by cracks advancement, consisting of a sequence of local failures in front of the crack tip, which are random events, caused or by the material local strength fluctuations (in inhomogeneous materials [69, 70]), or by existence of two or more alternating slip planes in crystal lattice; so that the crack trajectories behave randomly.

It is evident that in general case, the two-point correlation function (11) is insufficient to completely characterize the crack face morphology. More detailed description of crack faces morphology requires one to use the concept of multiaffinity that allows a mach more complete representation of real crack patterns by using an infinite hierarchy of scaling exponents. It has been shown that any random system F can be usefully characterized by an infinity spectrum of generalized dimensions D_q, where $-\infty < q < \infty$, also called the Rényi dimensions [58],

$$D_q = -\lim_{r\to 0}\left\{\frac{I_q(r)}{\ln r}\right\}, \qquad I_q(r) = -\frac{1}{q-1}\ln\left\{\sum_{i=1}^{N(r)} P_i^q(r)\right\}, \tag{20}$$

where $P_i(r)$ is the probability that a point of set under consideration lies in box (cell) number i such that

$$\sum_{i=1}^{N(r)} P_i(r) = 1. \tag{21}$$

The set $\mu = P_i$ is called multifractal probability measure or mass density, of the subset $F_i(r) \subset F$ contained inside the i-th covering box with the edge r; I_q is the generalized entropy of order q.

One can readily see that in the general case, D_0 is equal to the metric dimension evaluated by means of box-counting algorithm (see Table V), *i.e.*, $D_0 \equiv D_B = D_M$; the generalized dimension of order $q = 1$ is equal to the information dimension $D_1 = D_I$, which is associated with Shannon information entropy, that for a multifractal object scales as [9, 71, 72]

$$I(r) = -\sum_{i=1}^{N(r)} P_i(r)\ln P_i(r) \propto r^{D_I}; \tag{22}$$

and dimension D_2 is equal to the correlation integral exponent D_C, also called correlation dimension, which was introduced by Grassberg and Procaccia [73] as the exponent of a power-law correlation integral

$$C(r) = \lim_{N\to\infty} \frac{1}{N(N-1)} \sum_{i,j=1}^{N(r)} \Theta(r - \mid x_i - x_j \mid) \propto r^{D_C}, \tag{23}$$

where $\Theta(\cdots)$ is the Heaviside function. $C(r)$ counts the number of pairs of points such that $r < |x_i - x_j|$.

Note that for generalized Rényi dimension the following general relation [58] is valid:

$$D_{q'} \leq D_q, \qquad \text{for } q' > q; \tag{24}$$

the equality being obtained in the case of uniform sets, *i.e.*, such that the probability measure is constant, $P_i \equiv 1/N(r)$, and the generalized dimension D_q equals the metric dimension $D_B = D_H$ for all q; specifically, for homogeneous object all dimensions D_q are equal to the topological dimension, *i.e.*, $D_q \equiv D_H \equiv d_T$; and for self-similar fractals the definition in Eq. (20) gives $d_T \leq D_q \equiv D_0 = D_B \leq d$ for all values of q.

In some works (see, for example Refs. 74 and 75) have been assumed that for a uniform self-affine fractal $D_q = d - H$ for all q. Actually, however, the last equality is valid only in the case of monofractal structure for which the probability measure is constant $P_i \equiv 1/N(r)$. In the case of a self-affine fractal $P_i(r)$ will be the same for each box if we will use the covering network with affine rectangle (or elliptic) boxes which is associated with the elliptical dimension [64]; whereas when a network with the square or circular boxes is used $P_i(r)$ will be different for different boxes. Therefore for a self-affine fractal $D_{-\infty} - D_{\infty} > 0$.

To evaluate the generalized dimension spectrum of a self-affine fractal let us consider a self-affine fractal F in d-dimensional Euclidean space (for example a profile in plane such as shown in Figs. 7a or 7b). If $F_N \in F$ is a set of N points belonging to F and distributed over it in correspondence with an invariant measure, we can define the distance $\delta(N)$ between a reference point **A** and its nearest neighbor **B** among the $(N-1)$ other points. Evidently, $\delta(N)$ is a non-increasing function of N and, in general, some average over all points **A** will behave as $\langle\delta(N)\rangle \approx N^{-1/D}$. Badii and Politi [76] have introduced the probability distribution $P(\delta, N)$ of N distances among N points. The moments of $P(\delta, n)$ may be represented in the follows form

$$M_\gamma(N) = \langle\delta^\gamma(N)\rangle = \int_0^\infty P(\delta, N)\, d\delta = K(\gamma, N) N^{-\gamma/D(\gamma)}, \tag{25}$$

where $D(\gamma)$ is a γ-dependent definition of dimension, which called dimension function [76]. It was shown [77] that, whenever $\gamma = D(\gamma)$, *i.e.*, a fixed-point relation is satisfied, this value of the dimension function coincides with the generalized dimension, and

$$D\,[\gamma = (1-q)D_q] = D_q, \tag{26}$$

where D_q indicates the order–q Rényi dimension.

Equation (26) is valid for the some classes of systems obeying scaling behavior of the generalized entropy $I_q \propto r^{\tau(q)}$ within the interval of r bounded by the same value of the correlation length ξ_C for all q [4]. It is easy to understand that this condition is valid at least for the class of uniform self-affine fractals scaling properties of which within the interval $\ell_0 \ll r \ll \xi_C$ may be characterized by unique Hurst exponent H. Therefore, the evaluation of moments Eq. (25) allows the determination of any D_q by means of a recursive method: an initial value of γ is chosen to obtain a first estimate of the desired dimension which, in turn, is used as a new input until a satisfactory accuracy is reached.

Now, let us introduce the probability distribution function for the distances between these points

$$\Psi(R) = P\{\ell_{ij} < R\}, \qquad i, j = 1, 2, \ldots, N, \tag{27}$$

where $P\{\cdots\}$ is the probability that the distances ℓ_{ij} between any two points i and j of the N points is less than R. According to definition of the correlation integral $C(R)$ function $\Psi(R)$ is proportional to the correlation integral (23), namely

$$\Psi(R) = \frac{2N}{N-1} C(R) \propto R^{D_C}, \qquad R \ll \xi_C. \tag{28}$$

Let us determine the relation between probability function $\Psi(R)$ and dimension function $D(\gamma)$. By definition, Eq. (25), we have

$$D^{-1}(\gamma) = \lim_{N\to\infty} \frac{d[\ln \tilde{\Delta}(\Gamma) N]}{d(\ln N)}, \qquad \tilde{\Delta}(\gamma, N) = \left(\frac{1}{N} \sum_{i=1}^{N} \Delta_i^{\gamma} \right)^{1/\gamma}. \tag{29}$$

Here Δ_i is the distances from the point with index i $(i = 1, 2, \ldots, N)$ to its nearest neighbor point, and γ is the averaging exponent. The value of metric dimension D_H is defined by the Eq. (26) in the form $D(\gamma = D_H) = D_H$.

To calculate the mean distance to the nearest neighbor $\Delta(\gamma, N)$, let us find the probability distribution function for $\Delta(\gamma, N)$. The probability P_Δ that the nearest neighbor of a point A randomly chosen from the N points is located a distance R ($R \in [R, R+dR]$) away from it, and the remaining $N-2$ points are located outside a sphere of radius R centered at point A, is given by the equation

$$P_\Delta = (N-1)\Psi'(R)[1 - \Psi(R)]^{N-2}, \tag{30}$$

where P_Δ is the desired differential probability distribution function. As a result for the mean value $\tilde{\Delta}(\gamma, N)$ we have the expression:

$$\tilde{\Delta}(\gamma, N) = \left[\int_0^{\xi_C} P_\Delta R^{\gamma}\, dR \right]^{1/\gamma} = \left\{ \gamma \int_0^{\xi_C} [1 - \Psi(R)]^{N-1} R^{\gamma-1}\, dR \right\}^{1/\gamma}. \tag{31}$$

Using Eqs. (29) and (31), we obtain the expression

$$\tilde{\Delta}(\gamma, N) = \frac{1}{\sqrt[D_C]{L_C}} \left[\frac{\gamma}{D_C} \frac{\Gamma(N)\Gamma\left(\frac{\gamma}{D_C}\right)}{\Gamma\left(N + \frac{\gamma}{D_C}\right)} \right]^{1/\gamma}, \tag{32}$$

where $\Gamma(\cdots)$ is gamma function, and $L_C \simeq \xi_C^{D_C}$ is a normalization coefficient. If $\gamma = D_C$ the equality (26) with terms given by Eqs. (29) and (32) is satisfied and thus we obtain the equality $D_0 \equiv D_M \simeq \gamma = D_C \equiv D_2$. From this equality and general inequality (24) it follows that information dimension also equals the metric dimension D_M. The latter, as it has been shown in Refs. 64 and 78, related to the Hurst exponent as $D_M = d - H$ (see Table V). Thus we have shown that for self-affine fractals

$$D_C = D_I = D_M = d - H, \tag{33}$$

while $D_\infty \leq D_M \leq D_{-\infty}$.

Notice, that Eq. (31) may be used for the estimation of fractal dimension of a self-affine structure from data of experimental observations. In order to validate the Eq. (31) a line segment and two graphs of the Mandelbrot-Weierstrass function of known dimension were analyzed. To generate and evaluate the graphs of Mandelbrot-Weierstrass function the program [79] was used. It was found that the difference between theoretical values of fractal dimension and those calculated by using Eq. (31) is less than 0.5% for line segment and less than 3% for graphs of the fractal dimension $D = 1.4$ and $D = 1.8$.

It should be emphasized that equality (33) is valid for self-affine patterns obeying property (6) and power law behavior (22) and (23) within the same interval of length scales (17). For more complex patterns the interval of scaling behavior of the generalized entropy (20) is dependent on q. To characterize such a pattern we need to consider the qth order height-height correlation function [74, 75], defined as

$$G_q(x) = \frac{1}{N} \sum_{i=1}^{N} |z(x_i) - z(x_i + x)|^q, \tag{34}$$

where $N \gg 1$ is the number of points over which the average is taken (only non zero terms are considered).

For real multiaffine crack faces $G_q(x)$ exhibits a nontrivial multiscaling behavior

$$G_q(x) \propto x^{qH_q}, \tag{35}$$

with H_q changing continuously with q at least for some region of the q values [74]. It can be shown that a continuous spectrum of

$$H_q = \frac{1}{q} \lim_{x \to 0} \frac{\ln G_q(x)}{\ln x} \tag{36}$$

values is not consistent with the equality (14) which is valid only for uniform self-affine patterns with single exponent H; whereas for multiaffine patterns

$$C(x) \propto C^* x^{-(H_2 - H_0)}, \tag{37}$$

so that correlations between increments always vanish at large distances x. Therefore, experimental measurements of H in the scale of the order of ξ_C will always give the values which are closed to H_c. It seems to be the reason for results which lead to

TABLE VIII. The critical values of roughness (Hurst) exponent and various local fractal dimensions of crack face for d-dimensional problems of crack growth in the plane normal to applied tensile stress and in the direction of uniaxial compression.

Exponent	Crack growth in the plane normal to applied tensile stress[1)]		Crack growth in the direction of uniaxial compression[2)]	
	$d=2$	$d=3$	$d=2$	$d=3$
H_c	0.5	$\frac{2}{3}$	$\frac{1}{2}(\sqrt{5}-1)=\Phi^* \simeq 0.618$[3)]	
D_D^c	2	3	$1+\Phi^* \simeq 1.618$	3
$D_H^c = D_B^c$	1.5	2.333	1.382	2.382
$D_c^c = 2/(1+H_c)$	1.333	—	1.236	—
$D_c^c = \frac{1}{3}(10-7H_c)$	2	—	1.891	—

[1)] Critical values of exponents are corresponded to the brittle-ductile transition.

[2)] Crack growth is possible if the corresponding exponent less than its critical value.

[3)] Φ^* is the golden mean.

aforementioned conjecture about the universal roughness exponent.[4] The different values of H for different scales of the same crack face were observed in experiments [67, 80].

2.4. QUANTITATIVE CHARACTERIZATION OF MULTIAFFINITY

The absolute disorder of a large system is in principle impossible by virtue of the theorem of Ramsey, rigorously proved in number theory [81], according to which any sufficiently large quantity $N > R(N,n)$ of points (numbers, or objects) must contain a highly ordered subsystem of $N_n < R(N,n)$ elements [$R(N,n)$ are the Ramsey numbers]. Moreover, it has been shown that any random structure (or point set) consisting of a sufficiently large number of elements $N > B(N,n)$, where $B(N,n)$ is a certain set of numbers, can always be represented as a multifractal, consisting of a finite number n of the pre-fractals of i-generation ($i > n$) [3].

In this way, the concept of multifractals is related to the distribution of mass associated with a measure defined on the object which can be regarded in this way as a family of different homogeneous fractal sets on which the measure has a given singularity. To analyze the multifractality of a given object, the support of the measure is covered with boxes of size r^d and probability $P_i(r)$, which is the integrated measure, is computed in

[4]Notice that for three dimensional problems the critical value $H_c = 2/3$ (see Table VIII) coincides with the universal Hurst exponent, first suggested for the directed polymer problem, and then used as universal exponent for brittle fracture surfaces [79].

each box. The generalized dimension spectrum defined by Eq. (20) characterizes the non-uniformity of the measure.

In practice, sometimes it is more convenient to characterize multifractals not by dimensionality, but rather by spectral properties. The spectral function $f(\alpha)$ is defined by the number of hypercubes required to cover the subset $S(\alpha)$ with the same probability behavior $P_i(r) \sim r^{\alpha}(r \to 0)$:

$$dN_{\alpha}(r) = d\rho(\alpha)\, r^{-f(\alpha)}, \tag{38}$$

where α is the Lipschitz-Hölder exponent which characterized the singularities of the multifractal measure [58]. The relation between generalized dimensions D_q and spectral function $f(\alpha)$ is given by a Legendre transform: *the pair* $\{\alpha, f(\alpha)\}$ *is the Legendre transform of pair* $\{q, (q-1)D_q\}$. The obvious relation

$$\sum_{i}^{N} P_i^q \sim \int d\rho(\alpha) r^{\alpha q - f(\alpha)}, \tag{39}$$

leads, by the steepest descent method, to

$$D_q = \frac{1}{q-1} \min_{\alpha} \{\alpha q, f(\alpha)\} = \frac{1}{q-1}[\tilde{\alpha} q - f(\tilde{\alpha})], \tag{40}$$

with α defined by

$$\left.\frac{df}{d\alpha}\right|_{\tilde{\alpha}} = q(\tilde{\alpha}) \quad \text{as long as} \quad \left.\frac{d^2 f}{d\alpha^2}\right|_{\tilde{\alpha}} < 0.$$

The spectral function $f(\alpha)$ is widely used in the analysis of multifractals. Let us note one of its fundamental properties: if the spectral function is linear over some interval, this could indicate a phase transition that is difficult to detect by other means [58]. There exist a well-developed thermodynamic formalism for multifractals that emphasizes their close analogy to spin systems [4, 58].

Grassberg [73] has introduced a variant on Eq. (39) in which the measure is covered by a set of cubes of variable sizes, and has established a relation between the Rényi dimension D_q and the slope parameter $\tau(q)$ also called mass exponent which is defined by relation

$$\Sigma(q, r) = \sum_{i}^{N} P_i^q(r) \propto r^{-\tau(q)}. \tag{41}$$

The sequence of mass exponents $\tau(q)$ is related to the $f(\alpha)$ curve in a general way that is useful in applications. If we know the mass exponents $\tau(q)$, we can determine $f(\alpha)$ curve as

$$f(\tilde{\alpha}(q)) = \tau(q) + q\alpha(q), \tag{42}$$

where $\tilde{\alpha}(q)$ is the solution of equation

$$\frac{d}{d\alpha}\{q\alpha - f(\alpha)\}_{\alpha=\tilde{\alpha}(q)} = 0. \tag{43}$$

TABLE IX. Special values of the Rényi dimension, D_q, and corresponding values of $\tau(q)$, α, and $f(\alpha)$ for a multifractal measure $M = \{P_i\}$, supported by a set with fractal dimension $D_F = \dim_H M$, where $\dim_H M$ is the Hausdorff-Besicovitch (metric) dimension.

q	Dimension D_q	$\tau(q)$	$\alpha = -d\tau/dq$	$f(\alpha) = q \cdot \alpha + \tau(q)$
0	Fractal dimension $D_B = D_0 = \dim_H M$	$\dim_H M$	α_0	$f_{\max} = \dim_H M$
1	Information dimension $D_I = D_1$	0	$\alpha_1 = -I(r)/\ln r$	$f_I = \alpha_1 = I$ [1]
2	Correlation dimension $D_C = D_2$	$-D_C$	$-D_C - (dD_q/dq)_{q=2}$	$2\alpha_2 - D_C$
$+\infty$	Upper limit, D_∞	$\sim -q \cdot \alpha_{\min}$	$\to \alpha_{\min} = -\ln P_+ / \ln r$ [2]	$f \to 0$
$-\infty$	Lower limit, $D_{-\infty}$	$\sim -q \cdot \alpha_{\max}$	$\to \alpha_{\max} = -\ln P_- / \ln r$ [2]	$f \to 0$

[1] The measure M has entropy $I = -\lim I(r)/\lim r = f_I$, which is the fractal dimension of the set of concentration for the measure M. (Here $I(r)$ is the entropy of partition of measure M over boxes of size r).

[2] Here P_+ and P_- are the largest and the smallest probabilities in boxes of size r.

Therefore for the Lipschitz-Hölder exponent we have

$$\tilde{\alpha}(q) = -\frac{d}{dq}\tau(q). \tag{44}$$

These equations give a parametric representation of the $f(\alpha)$ curve, *i.e.*, the fractal dimension, $f(\alpha)$, of the support of singularities in the measure with exponent α. The $f(\alpha)$ curve characterized the measure and is equivalent to the sequence of mass exponents $\tau(q)$, which are related to D_q through

$$\tau_q = (1-q)D_q. \tag{45}$$

Some useful relationships between special values of D_q, $\tau(q)$, α, and $f(\alpha)$ are given in Table IX.

The next step in the standard strategy of multifractal analysis consists in resolving the exponent τ_q into a density of singularities $f(\alpha)$ with singularity strength $\alpha(q)$ [58]. In doing so, we obtain

$$\alpha(q) = \lim_{r\to 0}\left[\frac{\sum_{i=1}^{N} P_i^{(q)}(r)\ln P_i(r)}{\ln r}\right], \tag{46}$$

$$f(\alpha) = q\alpha(q) - \tau_q = \lim_{r\to 0}\left[\frac{\sum_{i=1}^{N} P_i^{(q)}(r)\ln P_i^{(q)}(r)}{\ln r}\right], \tag{47}$$

where the probability measure $\mu_q = \{P_i^{(q)}(r)\}$ is defined by the transformation $T(\mu, q)$ of the μ-measure included into the one parameter set $\{T_q\}$

$$T(\mu = \{P_i(r)\}, q) = \{P_i^{(q)}(r)\}, \qquad -\infty \le q \le \infty, \tag{48}$$

where the normalized measures $P_i^{(q)}(r)$ are defined as

$$P_i^{(q)}(r) = \frac{P_i^q(r)}{\Sigma(q,r)}, \qquad \Sigma(q,r) = \sum_{i=1}^{N} P_i^q(r). \tag{49}$$

It is easy to see that $P_i^{(1)}(r) = P_i(r)$ and

$$T(\{P_i^{(q_1)}\}, q_2) = T(T(\{P_i\}, q_1), q_2) = P_i^{(q_1 \times q_2)}, \tag{50}$$

so that we can define the identity T_1 and inverse $T_{1/q}$ transformations, because

$$T(\{P_i^{(q_1)}\}, q_2) = P_i, \quad \text{if} \quad q_2 = \frac{1}{q_1}. \tag{51}$$

Hence, the transformation defined by Eqs. (48) and (49) associates with the one-parameter group operating in the space of normalized measures, and the appropriate degree of difference between the μ and $T(\mu, q)$ measures may be characterized by the Kulback information [81]

$$K_q(r) = \sum_{i=1}^{N} P_i \ln \left[\frac{P_i(r)}{P_i^{(q)}(r)} \right]. \tag{52}$$

The Legendre transformation [82] of the function

$$\bar{\tau}(q) = \lim_{r \to 0} \frac{K_q(r)}{\ln r} \tag{53}$$

yields

$$\bar{\alpha}(q) = \frac{d\bar{\tau}(q)}{dq} = \alpha(q) - D_I, \tag{54}$$

$$\bar{f}(\alpha) = q\bar{\alpha}(q) - \bar{\tau}(q) = f(\alpha) - D_I, \tag{55}$$

$$\bar{\tau}(q) = \tau(q) - (q-1)D_I = (q-1)(D_q - D_I), \tag{56}$$

where $\alpha(q)$, $f(\alpha)$, and $\tau(q)$ are defined by Eqs. (41)–(45), and $D_I \equiv D_1$.

It immediately follows from Eqs. (33) and (24) that for a self-affine pattern

$$\bar{\tau}(0) = \bar{\tau}(1) = \bar{\tau}(2) = 0, \tag{57}$$

whereas for a multiaffine pattern

$$\bar{\tau}(0) = D_I - D_M < 0, \qquad \text{and} \qquad \bar{\tau}(2) = D_C - D_I < 0, \tag{58}$$

while, obviously, $\bar{\tau}(1) \equiv 0$.

In this way, the characterization of the non-uniformity of a multiaffine structure can be deduced by considering some degree of the order K_q. In fact, $K_q(r)$ may be referred to as a measure of nonuniformity of the multifractal structure. Its zero value corresponds to a uniform (statistically self-similar or statistically self-affine) pattern for which the transformation (48), (49) does not change the distribution measure, *i.e.* $T(\mu, q) = \mu$. A nonuniformity of multifractal and multiaffine patterns leads to non-zero values of the Kulback information $K_q(r)$.

Actually, the variation problem of finding the measure which corresponds to the entropy extremum [82]

$$-\sum_{i=1}^{N} P_i \ln P_i + \lambda \sum_{i=1}^{N} P_i + \sum_j \beta_j \sum_{i=1}^{N} P_i f_{ji} = \max \tag{59}$$

can be expressed in terms of the Kulback information as

$$-\sum_{i=1}^{N} P_i \ln \left[\frac{P_i}{\exp\left(\lambda + \sum_j \beta_j f_{ji}\right)} \right] = \max . \tag{60}$$

The last relation implies the minimization of the difference between distribution $\{P_i(r)\}$ and that meeting a certain set of constraints caused by two terms in Eq. (59). In our case from the comparison of Eqs. (60) and (52) follows that the corresponding variation problem can be formulated as follows:

$$K_q = -\sum_{i=1}^{N} P_i \ln \left(\frac{P_i}{P_i^{(q)}} \right) = \max, \qquad \text{where} \qquad P_i^{(q)} = \exp\left(\lambda + \beta \sum_j^{N} f_{ji}\right). \tag{61}$$

This provides an opportunity to use the function $\bar{\tau}(q)$ and, specifically, the parameters $\bar{\tau}(0)$ and $\bar{\tau}(2)$ as quantitative measures of the nonuniformity of multifractal and multiaffine structures, specifically, fracture surfaces.

From the analysis the experimental data reported [3] follows that in the case of brittle fracture

$$|\tau(0)| \ll H_0, \quad \text{and} \quad |\tau(2)| \ll H_0, \tag{62}$$

so we can put

$$H_0 \simeq H, \tag{63}$$

whereas for a ductile fracture surface

$$|\tau(0)| \sim |\tau(2)| \sim H_0, \tag{64}$$

so that the ductile fracture surface can not be characterized by the unique Hurst exponent.

Hence, in the case of brittle fracture we can use the self-affine representation for real (brittle) crack faces, while in the case of ductile fracture we have to use the concept of multiaffinity in the account to an adequate modeling of the real morphology of ductile fracture surfaces.

It would appear reasonable that in the case of intergranular cleavage the fractal dimension of crack faces is governed by the statistical topography of grain boundaries, and thus coincides with the fractal dimension D_g of grain boundaries. In the case of transgranular cleavage it should be reasonable to expect that the fractal dimension of crack faces D_B is less than D_g, so $H > d - D_g$. Path integral representation for self-affine patterns suggested in Ref. 12 to model a brittle crack paths was advanced in [63, 83]. Using this representation a detailed specification for the brittle crack morphology may be made on the basis of the Rieman-Liouville and Wigner-Valle spectra analysis [84] of the brittle crack profiles and surfaces.

It is important to note that the self-affine geometry of brittle crack faces leads to the change in the stress fields distribution in the vicinity of the crack tip and within the interval of self affinity (13) the value of stress singularity exponent is determined by the crack roughness exponent $H = d - D_B$ [10].

When the fracture is ductile, the crack morphology is governed by the kinetic of failure [5, 6, 14–18, 42] and possesses a multiaffine geometry which is characterized by a wide spectrum of generalized dimensions D_q for which the relations (64) are valid. In this case, the knowledge of crack faces metric dimension D_B is not sufficient to model crack faces morphology, which is quite different for different types (mechanisms) of ductile fracture, whereas for any ductile crack face with $D_B > D_B^*$ the stresses near the crack tip are constant within the interval (17) [12]. Hence, for the ductile fracture classification from the fractal point of view we need in more detail analysis based on the Kulback information concept. It would appear reasonable that the different types of ductile fractures may be classified in terms of suggested above parameters $\bar{\tau}(0)$ and $\bar{\tau}(2)$. This topic will be the subject of a forthcoming paper.

3. EXPERIMENTAL METHODS OF FRACTAL ANALYSIS OF FRACTURE SURFACES

The quantitative description of rough surfaces and interfaces has been an important challenge for many years. In the progress of science the ability to describe phenomena in precise quantitative terms frequently leads to important advances in understanding. This certainly seems to be true in the case of fracture surface formation. In the review [85] Nowicki has described 32 parameters and functions that have been used to characterize rough surfaces. It is important to classify phenomena so that the task of describing and understanding them can be reduced to a reasonable magnitude. In recent years it has been realized that fractal geometry and scaling concepts can considerably simplify this task for a quite wide range of systems including fracture surfaces. In this way, the main purpose of fractographic investigations is to determine the fractal dimension of fracture surface and the limits within which the surface exhibits fractal properties. Of course, for a dimension to have any significance, repeating an experiment must lead to the same value!

In general, fractal analysis provides a description of how space is occupied by particular curve or shape. The fractal dimension measures the relative amounts of detail or "roughness" occurring over a range of measurement intervals. The more tortuous, convoluted and richer in detail the curve, the higher fractal dimension. However, rough-

ness and fractal dimension are not synonymous. Roughness is generally measured as the average variation about the mean value, and is not related to the scale or changes in scale of measurement. Fractal dimension is used to quantify the variation of the length or area with changes in the scale of measurement interval. Hence the fractal dimension is an intensive property (see Tables I–V), while roughness is not.

In order to investigate the fractal properties of a rough fracture surface, it is necessary to determine its area as a function of measurement length. Several techniques have been developed for these measurements [3, 58]. In principle, stereophotogrametry should more or less provide an adequate topographic description of rough surfaces. Provided the computer used has enough memory, this very rich information can be analyzed to measure the fractal dimension of the surface. A technique which provides a similar information, although in a very different length scale domain is the scanning tunneling electron microscopy. In practice, however, more commonly the one or bi-dimensional cuts of fracture surface are studied by using the fractographic methods [3].

Fractographic methods used to obtain fractal information from rough fracture surfaces, involve either obtaining surface profiles from metallographic sections cut perpendicular to the surface plane *(vertical section method)*, or from sequentially prepared sections parallel to the surface plane *(slit island method)*, or from spectral analysis of roughness of surface *(spectral methods)* [3]. Usually, an additional hypotheses is needed in order to achieve relation between fractal properties of surface and its cuts.

One of the most critical problems of fractal measurement and applications is the ability to recognize and correctly measure the fractal dimension of self-affine fracture surfaces. The horizontal contours of a fracture surface may be statistically self-similar, but the vertical profiles are commonly self-affine [3]. Hence, the horizontal and vertical cuts of a fracture surface have quite different scaling properties which must be estimated by means of different measurements.

For statistically self-similar horizontal contours any reasonable procedure of fractal measurement should lead to the same value of fractal dimension. The question is *how this fractal dimension relates to the fractal properties of self-affine (or, generally, multiaffine) fracture surface?*

For self-affine vertical profiles, there are many different fractal dimensions, some local and global. The later always equals the topological dimension of profile, while the local dimensions may be expressed as functions of the roughness exponent H (see Table V).

Methods for measuring self-affine roughness exponent can be schematically cast into two groups. One find the classical methods, developing for analyzing self-similar fractals: box-counting, divider, perimeter-area relation, power spectrum scaling, which provide the different fractal dimensions for a self-affine surface. Several other methods sometimes used in practice of fractal measurements. That are *chord-length measurements* [88], *variogram method* [89], and *correlation function measurement* [90]. On the other hand, several methods have been designed to specifically determine the self-affine exponents: *a variable bandwidth method* [29] and *return probability method* [86, 87].

Various experimental techniques are used for fractal analysis of fracture surfaces. Among them, the scattering techniques (small-angle neutron scattering [3, 58], optical diffraction experiments [3], and secondary-electron emission measurement [58]), fractographic studies [3, 78], adsorption-desorption studies (adsorption probes method [58], and

thermodynamic method [91]), deposition experiments [92], electro- and heat-chemical methods [93], nuclear magnetic resonance pore-size distribution measurement [88], and some indirect methods, such as skin effect measurement and charge relaxation measurement [3], etc.

Below, some of the most important fractographic techniques and methods of fractal measurement are discussed in more detail.

3.1. SLIT-ISLAND TECHNIQUE

The slit-island technique was first introduced by Mandelbrot *et al.* [8] who applied it to the fractal analysis of steel fracture. The filled steel fracture surfaces with nickel (by electrolytic deposition), then polished the fracture surfaces parallel to the mean fracture plane, so that approximately equal amounts of nickel and steel were evident on the polished fracture faces. This created a pattern of islands of nickel in a sea of steel, which was called "slit-islands." Instead of nickel, a plastic material may be also used [3, 58]. The fractal dimension measurement by means of slit-island technique is based on the analysis of perimeter (P)-area (S) relations for the islands surrounded with coating material.

It is well known, that for circles, ellipses and regular polygons, the ratio of the perimeter to the square root of the surface area embraced by this perimeter is independent of the figure size:

$$k = \frac{P}{\sqrt{S}} = \text{const.} \tag{65}$$

Thus, for circles, $k = 2\sqrt{\pi}$, for squares, $k = 4$; for equilateral triangles, $k = 6\sqrt[4]{3}$; etc.

In the case of fractal profile of the island perimeter, its length P is dependent on the type of standard δ used in measuring P; in this case, at $\delta \to 0$, the perimeter grows infinitely:

$$P(\delta) \to \infty \quad \text{when} \quad \delta \to 0.$$

In contrast, the island area $S(\delta)$, measured by its covering with squares with side δ, remains finite at $\delta \to 0$. The typical $\ln S$-$\ln P$ plot obtained in studies of fracture surfaces by slit island method is shown in Fig. 8. The slope of the curve (plotted by applying the least squares method) is determined by the fractal dimension D_f of the statistically self-similar island contour

$$\alpha_Y = \frac{2}{D_f}. \tag{66}$$

So for islands with a fractal coastline, the ratio Eq. (65) should be replaced by the following parameter

$$k_F = \frac{\sqrt[D_F]{P(\delta)}}{\sqrt{S(\delta)}}, \tag{67}$$

which is independent on the size of the island and δ.

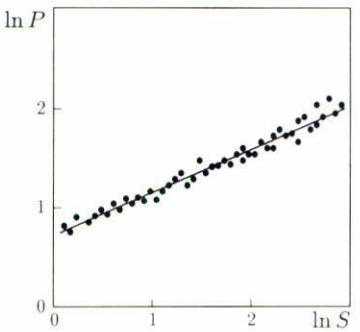

FIGURE 8. The fractal area-perimeter relation for slit islands on fracture surface of 30CrMnSiNi$_2$A steel fractured at -20°C (graph adopted from Ref. 39): $[P] = \mu$m, $[S] = \mu$m^2.

The fractal dimension of statistically self-similar surface relates to the fractal dimension of the island's perimeter by empirical relationship

$$D_F = 1 + D_f = 1 + \frac{2}{\alpha_Y}, \tag{68}$$

known as one of Mandelbrot's "rules of thumb" for fractal sets [58].

Actually, relation (68) is valid only for some specific cases of statistically self-similar surfaces [58]. Generally, the fractal dimension of statistically self-similar surface $D_F \geq D_f + 1$ [94], so Eq. (68) gives only the lower limit for the fractal dimension of the self-similar surface. For example, in Fig. 1b–c we have show three different fractals of different fractal (metric) dimension whereas for all these fractal the baseline cross-section is homeomorphic to the Cantor set (Fig. 1a) with fractal dimension $D = \ln 2/\ln 3$.

Furthermore, as it was noted in the previous section, real fracture surfaces are rather statistically self-affine than self similar. Hence Eq. (68) can not be used. If a fracture surface is isotropic in the mean plane, then the slit-island pattern will be statistically self-similar, and so for a selected cutoff it may be characterized by the fractal dimension D_f, while $H \equiv 1$. Moreover, generally, D_f will depend on the cutoff choice.

On the other hand, to determine the perimeter-area relationship we can use different cutoffs, but the same measurement length δ_0. In this case the slope of the $\ln S$-$\ln P$ plot determines the contour fractal dimension D_{cn} (see Table V). If surface is self-similar then $H = 1$ and $D_{cn} = D_f$, while for self-affine surface $H < 1$ and D_{cn} relates to the Hurst (3) exponent as

$$D_{cn} = \frac{2}{\alpha_Y} = \frac{2}{1+H}. \tag{69}$$

So, the metric dimension of statistically self-affine surface D_M is related to D_{cn} by the equation

$$D_M = 3 - H = \frac{2(2D_{cn} - 1)}{D_{cn}} = 4 - \alpha_Y, \tag{70}$$

which should be used instead of the commonly used incorrect Eq. (68). In Fig. 9 we show the dependence of the surface metric dimension D_M on the α_Y calculated by Eqs. (68)

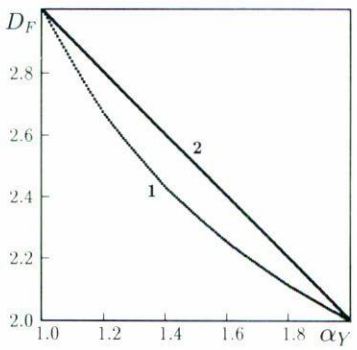

FIGURE 9. The relation between fractal dimension of self-affine surface and the slope of area-perimeter plot in log-log coordinates (of the type shown in Fig. 5). Curve 1: calculation by classical formula (68) and curve 2: calculations by Eq. (70).

and (70). As we can see, the values of D_M calculated by Eq. (68) will be always less than those calculated by Eq. (70) when the same data for $1 < \alpha_Y < 2$ are used. Hence the data reported in the literature, which were obtained by slit-island measurement, should be corrected.

Notice, that Eqs. (69) and (70) are valid only for self-affine fracture surfaces which are isotropic in mean plane. It was shown [95] that the slit-island technique is insensitive to anisotropy in the plane of fracture and so it is useless when the slit-island pattern is also self-affine.

3.2. VERTICAL SECTION TECHNIQUE

A very useful experimental procedure for fractal measurement of anisotropic fracture surfaces is based on vertical section through the surface The sections generate profiles (see, for example Figs. 7a and 7b) that sample continuously across the entire surface as opposed, for example, to the point-by-point registration obtained by stereophotogrametry measurements. With the sample in a metallographic mount, the fracture path and underlying microstructure are revealed in relation to each other, and the standard equations of stereology are applicable to both. Moreover, serial sectioning is readily performed merely by grinding down the face of the sample parallel to the previous location. This procedure yields a new profile each time and systematically samples through sample space. Accordingly, equation

$$L = L_0 \Delta^{1-D_p}, \tag{71}$$

where L_0 is a constant and the value of the non-integer exponent D_p, which is independent of the measuring step size Δ, is normalized by the projected length of the profile, L_p.

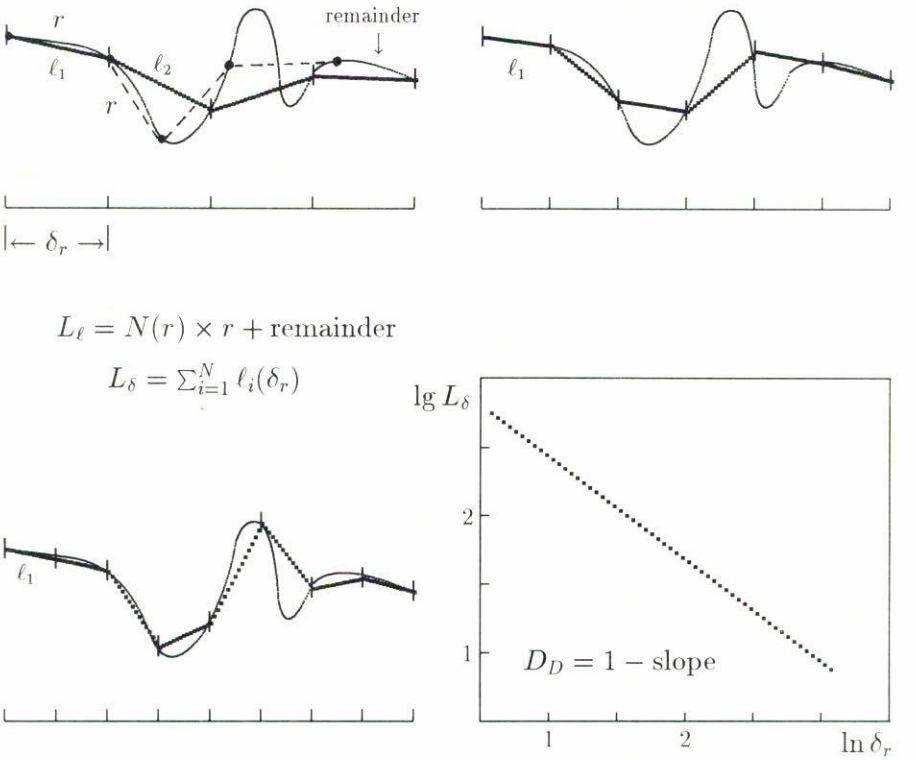

FIGURE 10. Schematic illustration of divider measurement of the profile length with variable stick (divider, ruler) length.

There are basically three methods for measuring fractal dimension of profiles:[5] (1) the divider (or yardstick, or ruler, or compass) method, (2) linearization of reversed sigmoidal curves method, and (3) the box-counting method.

3.2.1. The divider method

It is the oldest method of determining the fractal dimension. Its use as a measurement technique predates the invention of the word "fractal." The basic method involves measuring the length of a curve either at different resolutions, or with different sizes of measuring stick (ruler, caliper). Another name for this method is the structured walk technique. The essential characteristics of this method are illustrated in Fig. 10. First walk the stick along the profile and record the length (which equals the number of stick lengths times the size of the stick). Next, change the length of the stick and repeat the measurement. Repeat this process several times, each time with a different stick length. Then plot the log of the curve length versus the log of the stick length. If the data plot along a straight line, this means that the profile has fractal geometry. This plot is sometimes called a *"Richardson plot."* The results of grain boundary length measurements by using divider method are shown in Fig. 5b.

[5]The fractal dimension of profile can be also estimated by using Eqs. (30)–(32).

Now, determine the slope α_Y of the line which best fits the data, and compute the fractal dimension of the profile from this slope using relation

$$D_p = 1 - \alpha_D = D_D. \tag{72}$$

For self-affine profile D_p is related to H as $D_p = D_D = 1/H$ (see Table V) and the metric dimension of surface relates to α_D as

$$D_M = 3 - H = 3 - \frac{1}{D_p} = \frac{2 - 3\alpha_D}{1 - \alpha_D}. \tag{73}$$

In practice, however, there are several operational problems which are associated with the choice of the length scale resolution. A self-affine profile scales differ in the horizontal and vertical direction. If horizontal resolution is near the crossover length, than the divider method may give invalid results. Hence, before performing the fractal measurement by the divider method, it would be very useful to know whether or not the surface is self-affine.

To do this, we need to calculate the standard derivation (4) for the X and Z coordinates for many pair points in the profile. A fixed stick scale should be used to measure the length between each pair of points. Then the coordinates of all of the measurement points of the stick are used to calculate two standard derivations (4) in the two coordinate directions. These standard derivations for all pair of points mast be plotted versus length on log-log scale. The slopes of these two lines yields the self-affine exponents ν_x and ν_z defined by Eq. (5). If $\nu_z = \nu_x$ then the profile is statistically self-similar and $D_D = 1/\nu_x = 1/\nu_z$, whereas for self-affine profile $\nu_x \neq \nu_z$ and the Hurst exponent H is defined by Eq. (3).

Another operational problem is the problem of remainder. For the divider method, as one approaches the end of the profile, there will be some quantity which won't fill the last stick. This results in the error in the length estimation. Three ways are suggested for handling the remainder [3].[6] One way is to use only those rules which give a remainder less than a specified value of tolerance. A second way is to add the straight-line distance between the stick and the end of the profile to the total length. A third way is to round up the remainder. Choosing a method for handling the remainder may lead to different estimates of fractal dimension D_p, and these differences should be treated as part of the error of the measurement.

3.2.2. The linearization of reversed sigmoidal curves method

It is based on the studies of surface roughness parameters. It has become evident in the study of fracture profiles that the profile roughness parameter, R_z, occupies a central position in expressing the characteristics of the profile. The parameter R_z is defined by the length $L(\Delta)$ of the fractal curve, which approximate the profile with stick Δ, divided by L_p, the (constant) profile projected length. It also bears a direct relationship to R_s, the surface roughness parameter, which is defined by the surface area S_s divided by its

[6]The slit-island method also has a remainder problem [3]. What happens to islands which cross the boundaries of the region of study? Should they be ignored, or partially counted?

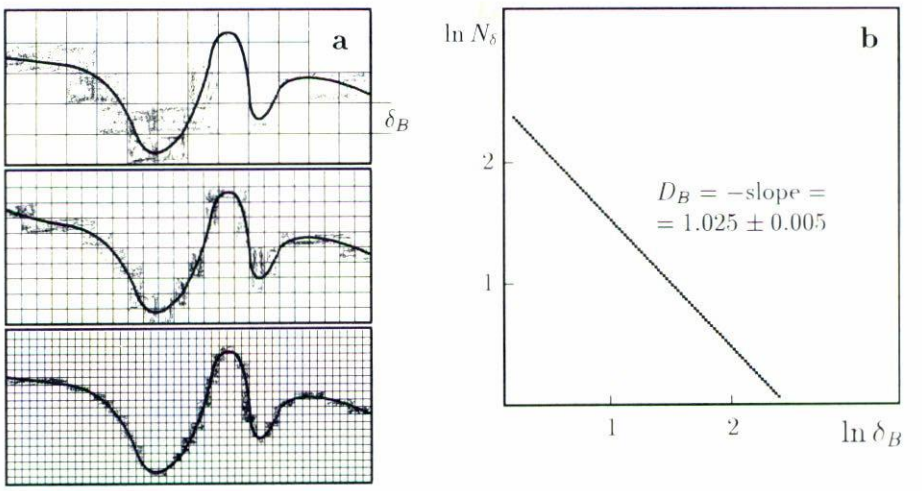

FIGURE 11. Schematic illustration of the box-counting measurement (*a*); the plot of the number of boxes needed to cover the fracture profile in Cu *versus* box size (*b*). Experimental data adapted from Ref. 3.

projected area, S_p. Although R_s is the quantity sought because it gives the fracture surface area, it is relatively difficult to obtain. The parameter, R_z, on the other hand, is an experimental quantity that is measured directly from a vertical section [1–3].

Several analytical methods have been proposed for determining R_z. One of the simpler ways is through the linear parametric equation that links R_s directly to R_z according to empirical equation

$$R_s = \frac{4}{\pi}(R_z - 1) + 1. \tag{74}$$

This relationship provides the best fit to all known experimental data [1]. It is based on a realistic model, that is, a fracture surface that can have any configuration between the limits of completely oriented $(R_s = 1)$ and extremely complex $(R_z \to \infty)$.

If the approach of marking segments along a baseline is used instead of marking segments on the profile, than the remainder problem can be avoided by recursively subdividing the total length of the baseline into halves. In analyzing the fractal behavior of irregular fracture surfaces, data point pairs (R_z, R_s) are needed for each configuration. Equation (74) supplies the inaccessible quantity, R_s, with a high degree of reliability and a minimum of calculation. This method was described in detail in Refs. 1, 3, and 96.

3.2.3. The box-counting method

It uses boxes to measure the length of a profile, or the density of the lines or points over an area. The curve is covered with square boxes as shown in Fig. 11a.

The size of the box l_B is the length of the square. The number of same sized boxes needed to cover the line is counted. This is repeated for series of different sized boxes. The result are then plotted as the number of boxes N_B (Y-axis) *versus* l_B (X-axis)

on a log-log plot as shown in Fig. 11b. The fractal dimension of line (profile) is equal to the slope of the plot, *i.e.*,

$$D_p = D_B = 2 - H = -\alpha_B, \tag{75}$$

where α_B is the slope of the plot. A variation of this method is to use circles instead of squares, where the diameter of the circle is equivalent to the box size. The box method can be modified for self-affine curves by converting the square boxes to rectangles which have an aspect ratio representing the ratio of the anisotropic scaling factor.

There are different ways of applying the box-counting method for measurements of fractal dimension. This method can be easily implemented with a computer algorithm by defining the boxes with a square grid. To handling a potential remainder problem, one can then count the number of intersections of the line with the boxes (grid elements or tiles), or alternatively, the number of boxes intersected by the line. When using a computer, one can start with the finest resolution image and then mathematically combine tiles into larger, lower resolution images, a procedure called "mosaic amalgamation." The box method can be used to analyze areas within curves as well as the curve itself. One can apply the centroid rule where the centroid of the box has to lie in the region of interest (non on the other side of the line) for the box to be counted. One can also apply the "majority rule," where a box is counted if more than half of its area lies within the region of interest [3].

Obviously, the evaluation of D_p depends on the method and algorithm used, on the range chosen, on the sequence and the scale resolution on the analyzed profile. Hence, the estimated fractal dimension is not an absolute measure so those parameters must always be specified in order to reproduce the results as well as to compare and interpret them.

3.3. TESTING FOR SCALING

The problem of estimation of the slope from the $\log Y$-$\log X$ plot is common for all methods of fractal measurement. When we are dealing with uniform self-similar or self-affine patterns there are no problems. The log-log plots are linear at least on the average. When, however, we are working with real fracture surfaces, problems begin to emerge. In fact, scaling is assumed *a priori* and the scaling region is subjectively estimated. In this way, there is no consistent way of estimating the slope and different methods can give considerably different results!

The slope may be estimated by a linear regression, or other standard curve-fitting techniques. Often, only part of the plot is used to calculate the slope, while other researchers will use the entire plot. The slope is often somewhat curved, rather than straight (see, for example, Refs. 1, 3, and 80). Does this curvature indicate that the fractal theory is not applicable to that particular data set, or is this just the expression of lack of self-similarity of the data? What does it mean if the curve is concave up versus concave down? Some researches choose a particular straight section of the curve for the estimation of slope, explaining that the straight segment is the range of scales over which the fractal theory applies. If an error analysis were applied to the slope estimation, the error range for the fractal dimension could be as large as the possible range of fractal

dimensions. Many of the studies do not estimate errors, or they estimate only one aspect of the error, such as the curve-fitting error, while ignoring other such as the remainder error.

If the slope α is determined with the help of the least-square fit, the standard deviation of the fit may be interpreted as the error bar of the obtained dimension value. However, the error bar defined in such a way does not reflect the uncertainty of the calculated value of fractal dimension due to the finiteness of data set, but it is rather related to the choice of the fitting range.

Actually, position of each point in the log-log plot is determined by the relation $\log N/\log r$, where $N(r)$ is the number of sticks (boxes) with size r needed to cover the evaluated profile. To obtain an exact result, the limit $N \to \infty$ should be achieved. In practice, we always have a finite set of $N(r)$ points. Hence the underlying question being: how many data points are needed in order to obtain a "correct" estimate of a given slope. It is clear that the higher the fractal dimension of profile, the greater number of points N needed in order to correctly evaluate the slope of the log-log plot. Several empirical criteria have been suggested in the literature, which define the minimal number of data points N required for a "reliable" estimation of a given fractal dimension D [97, 98]. They have the form

$$N \gg 10^{D/2}, \qquad \text{and} \qquad N \geq 42^{D}. \tag{76}$$

Of course these limitations are in some sense subjective, but they are very useful in the practice of fractal measurement [3]. However, in this approach, the question of whether a given data set is self-similar (self-affine) is overlooked.

The authors [99] have suggested the tests of self-similarity and self-affinity based on the data analysis in the coordinates $\log(dY/dx)$-$\log X$ which gives the slope α as the function of the logarithm of measurement scale length. For a uniform fractal $\alpha =$ constant. The fracture surface can be treated as a statistically self-affine object only when the corresponding slope α varies within a certain bounded interval (for example, the 5%-95% interval of the observed frequency distribution of α).

Here, we suggest another test for self-affinity which is based on the comparison of the values of roughness exponent H obtained by divider $H^{(D)} = 1/(1-\alpha_D)$ and box-counting $H^{(B)} = 2 - \alpha_B$ methods. For a uniform self-affine pattern, obviously,

$$H^{(H)} \equiv H^{(D)}.$$

Furthermore, as it follows from the analysis in Subsect. 2.4, if

$$|H^{(B)} - H^{(D)}| < \frac{1}{D_D} \min\left\{H^{(B)} = 2 - D_B, H^{(D)} = \frac{1}{D_D}\right\}, \tag{77}$$

then the fracture surface can be treated as self-affine and so may be characterized by the unique roughness (Hurst) exponent

$$H = \sqrt{H^{(B)}\, H^{(D)}}. \tag{78}$$

Otherwise, the surface must be considered as multiaffine and we need to estimate parameters $\bar{\tau}(0)$ and $\bar{\tau}(2)$ to its characterization.

In order to validate the criterion (77), two self-affine graphs of the Mandelbrot-Weierstrass function with $H = 0.5$ and $H = 0.8$, and the graph of deterministic multi-affine function [74] were analyzed. To generate and evaluate the graphs of Mandelbrot-Weierstrass function the Fractal Vision software [79] was used. For the graph with theoretical value of Hurst exponent $H = 0.5 (D_D = D_B = 2)$ it was found $H^{(D)} = 0.53$ and $H^{(B)} = 0.48$ so that inequality (77) is valid and by Eq. (78) we obtain value $H \simeq 0.5$ which coincides with the theoretical one. For graph of Mandelbrot-Weierstrass function generated with $H = 0.8$, $D_D = 1.25$ we found $H^{(D)} = 0.85$ and $H^{(B)} = 0.78$, and so, the inequality (77) is also valid. For the graph of deterministic multi-affine function described in [54] we obtain $H^{(D)} = 0.5$ and $H^{(B)} = 0.85$, so that $|H^{(B)} - H^{(D)}| = 0.35 > 0.5H^{(D)} = 0.25$. Hence, the scaling properties of this function can not be characterized by a single Hurst exponent.

4. Fractal properties of fracture surfaces in steel 1045

The material chosen for the experimental studies of fracture surfaces topography was the steel 1045 widely used in industry [1, 3, 100]. In order to validate the suggested concepts, specifically, the test of self-affinity and non-universality of the fracture roughness exponent H, the mechanical tests were made at different temperatures and for different strain rates.

4.1. Mechanical testing

Tensile bars were machined from heat treated samples to a 5 mm diameter and a gauge length of 50 mm (length/diameter = 10 coincides with german standard [101]). The bars were tested in accordance with the standard tension test (ASTM E8-81) using the INSTRON tensile apparatus (model 1125). Tension tests were made at different temperatures (when temperature was raised over 300°C, the atmosphere pressure was kept at 10^{-6} torr), and for different strain rates: 3.333×10^{-5} s^{-1}, 3.333×10^{-3} s^{-1}, 1.666×10^{-2} s^{-1}, and 1.666×10^{-1} s^{-1}. The ultimate tensile strength, σ_c, elongation, δ_p, and adsorbed energy, E_a, for each sample was calculated from the results of these tests. The typical example of stress-strain diagram is shown in Fig. 12a. The variations of the σ_c, δ_p, and E_a with the testing temperature are shown in Figs. 12b, 12c, and 12d, respectively. We can see that mechanical properties of steel 1045 change dramatically in the interval 500–800°C, while their variations within the intervals 25–500°C and 800–1000°C are insignificant. Hence, it is reasonable to expect that the fractal properties of fracture surface also will possess changes in the interval 500–800°C. Furthermore, it is reasonable to expect the changes in fractal properties associated with a dramatical decrease in adsorbed fracture energy in tests with strain rate 3.333×10^{-5} s$^{-}1$ (see Table X).

4.2. Fractal measurements

After mechanical testing fractured specimens were assembled in baseline and fracture surfaces were covered by epoxic resin. Then specimens were machined to obtain the

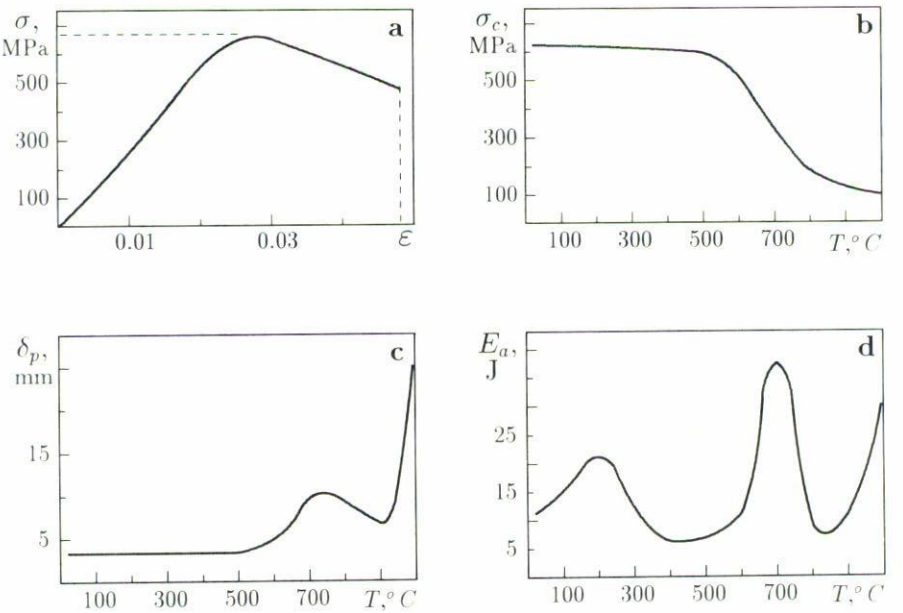

FIGURE 12. The stress-strain diagram for steel 1045 at 300° C obtained in the tensile test with strain rate $3.333 \times 10^{-3}\text{s}^{-1}$ (a); and the temperature behavior of the ultimate tensile stress (b), elongation (c), and adsorbed energy (d).

vertical cut profiles which were microphotographed to 200× and 500×. All microphotographs were scanned in Studioscan IIsi-AGFA and obtained scanning profiles were used for fractal measurement. Figs. 13a and 13b show the micrographs of rupture profiles for two specimens fractured at temperatures 300°C and 500°C, respectively. The fractal dimension of each profile were estimated by means of divider and box-counting methods. Obtained in such a way data were used to calculate the values of roughness exponents $H^{(B)}$ and $H^{(D)}$. Thereupon, if the inequality (77) is valid, the Hurst exponent H were calculated by Eq. (78).

4.3. DIVIDER MEASUREMENT

The foundations of divider dimension measurement by means of yardstick (divider method are described in Sect. 3.2.1). The main operational problem associated with this measurement is the problem of remainder. In present work this remainder was handled by adding the straight-line distance between the ruler and the end of analyzed profile to the total length (see Sect. 3.2.1).[7] The interval $10 \div 10^3$ mμ was chosen for the ruler length δ_r, so that according to criteria (76) the number of data points were sufficient for a reliable estimation D_D. Only the points associated with ruler length $\delta_r < \xi_C$ were used to estimate the slope of the plot in the coordinates $\log L_p$-$\log \delta_r$ by the least square

[7]The algorithm of measurement was tested by the evaluation of the graphs of Mandelbrot-Weierstrass function generated by the program [79]. In all cases the difference between theoretical and estimated values of H was less than 8%.

TABLE X. Adsorbed energy and fractal properties of fracture surfaces in steel 1045 fractured in standard tests with strain rate 3.333×10^{-3} s^{-1} at different temperatures.

T(°C)	E_a, J	$H^{(B)}$	$H^{(D)}$	H, Eq. (78)
25	1.35	0.958	0.959	0.958
100	14.56	0.961	0.960	0.960
200	19.44	0.955	0.930	0.942
300	8.97	0.940	0.917	0.929
400	9.36	0.935	0.915	0.925
500	6.99	0.820	0.910	0.864
600	11.86	0.805	0.846	0.825
700	37.96	0.950	0.951	0.950
800	8.81	0.972	0.973	0.972
900	7.79	0.971	0.972	0.971
1000	0.972	0.996	0.970	0.971

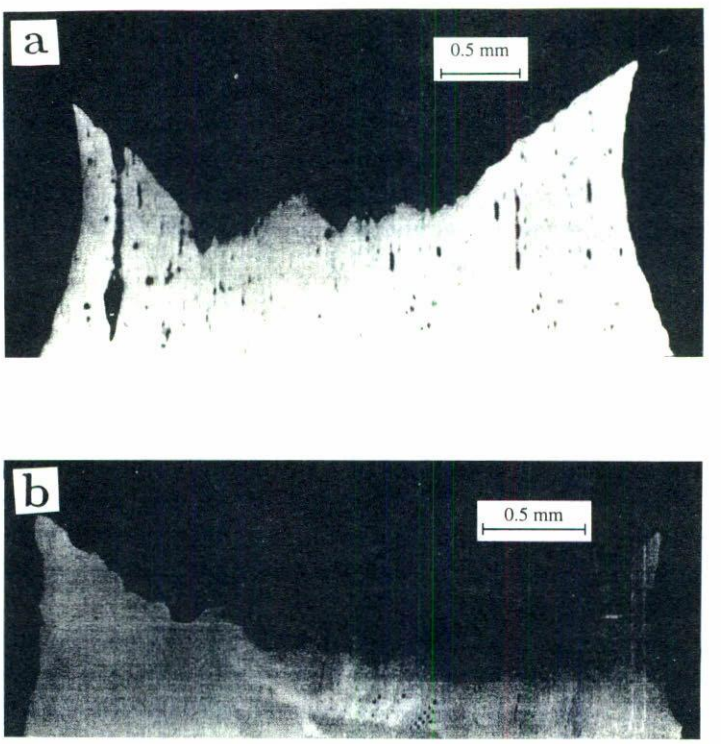

FIGURE 13. Micrographs of fracture profiles in steel 1045 fractured at temperature 300°C (a) and 500°C (b) with testing strain rate 3.333×10^{-3} s^{-1}.

TABLE XI. Adsorbed energy and fractal properties of fracture surfaces in steel 1045 fractured at 1000°C in the standard tests with different strain rates.

Property	Strain rate (s^{-1})		
	1.666×10^{-1}	3.333×10^{-3}	3.333×10^{-5}
E_a, J	30.253	29.960	5.320
D_D	1.041	1.030	1.171
$H^{(D)}$	0.961	0.970	0.853
D_B	1.041	1.028	1.140
$H^{(B)}$	0.956	0.972	0.960
H, Eq. (78)	0.960	0.971	0.857

method. The method of the ξ_C estimation is easy to understand from Figs. 11a and 11b which show two typical plots of divider measurements. The corresponding values for divider dimension and $H^{(D)}$ were calculated by Eqs. (72) and (77), respectively. These data are listed in Tables X and XI.

4.4. BOX-COUNTING MEASUREMENT

The foundations of box-counting fractal measurement are described in Sect. 3.2.3. To avoid the problem of remainder we have used the box-counting algorithm suggested in Ref. 102.[8] Two typical plots of box-counting measurements are shown in Figs. 14c and 14d in coordinates $\log N(\delta_B)$-$\log \delta_B$. Estimated by the least square method the slope of a plot was used to calculate the box-counting dimension and $H^{(B)}$ by Eq. (75). Obtained in this way data are listed in Tables X and XI.

4.5. DISCUSSION

Generally, different methods of fractal measurement lead to the same fractal dimension only for a statistically self-similar fractal. At the same time, different methods of fractal measurement of the vertical cross-sections of a statistically self-affine surface should give the same value of the roughness (Hurst) exponent, if they applied correctly. Multi-affinity of real fracture surfaces manifests itself in the difference between Hurst exponents estimated by different methods. In this way, the self-affinity of real surface can be verified by using criteria (58), (62), and (77).

As it is easily seen from data in Tables X and XI, for all investigated fracture surfaces the inequality (77) is valid, and so they may be treated as statistically self-affine fractals within the interval (17) and characterized by the unique roughness (Hurst) exponent (78). In this way statistically self-affine fracture surfaces in steel 1045 can be advantageously modeled by the homeomorphic regular self-affine fractals (for more details see section 2).

[8]The algorithm was tested in [102] and it was shown that it gave the best results in comparison with other common algorithms.

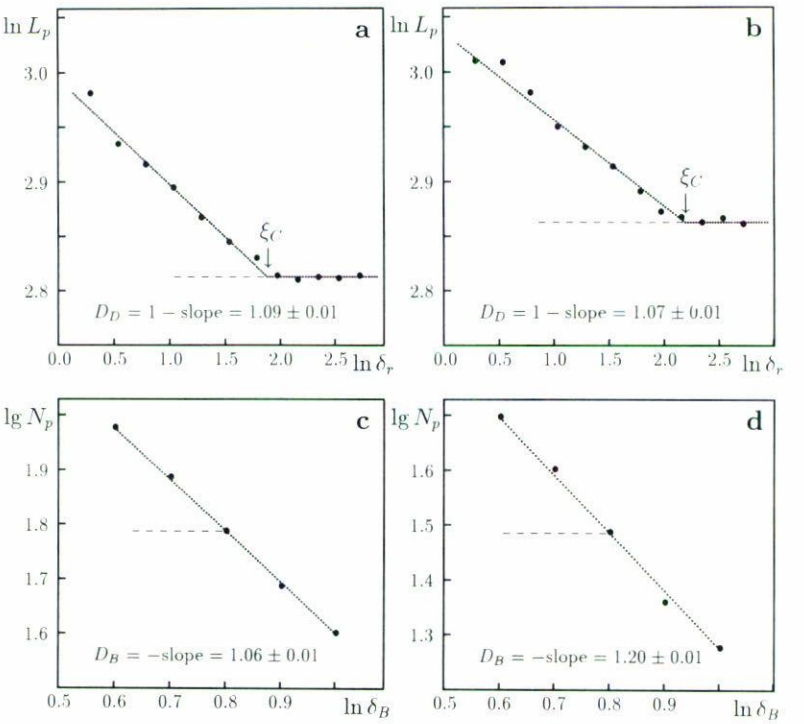

FIGURE 14. Length of fracture profiles L_p shown in Fig. 13a and 13b plotted *versus* stick length (a, b) and the number of boxes covered these profiles N_p plotted versus box size (c, d). Graphs a and c are related to the profile in Fig. 13a ($\xi_C = 0.31$ mm) and graphs b and d are related to the profile in Fig. 13b ($\xi_C = 1.06$ mm).

While no clear relation has been found between H and the studied mechanical properties, it is clear from data presented in Tables IX and X that the changes in fractal properties coincide with those for mechanical properties. Hence our data cast doubt on the hypothesis of universality for fracture roughness exponent. To obtain explicit interrelations between mechanical properties of a material and fractal properties of fracture surfaces, we need in a more presentable set of experimental data. Specifically, it seems to be interesting to investigate the relation between adsorbed energy and fractal properties of fracture surface for different strain rates of mechanical testing.

5. CONCLUSIONS

In this work the fractal approach to fracture surface morphology characterization was advanced.

It is noted that while, explicitly speaking, real fracture surfaces are always multifractal or multiaffine, in some cases they can be treated as statistically self-similar (or self-affine) pre-fractals obeying scaling properties within a wide but bounded lengthscale interval (17). The criteria (58), (62), and (77) and quantitative characteristics (53) of multifractality (multiaffinity) are suggested.

It is important to keep in mind that any random (statistically self-similar or statistically self-affine) fractal can be transformed in the regular fractal with the same fractal (metric) dimension by a homeomorphic, one-to one and onto transformation. Hence, regular and random fractals of the of the same fractal dimension are statistically equivalent and cannot be distinguished within a framework of fractal geometry. In this way statistically self-similar (self-affine) fracture patterns can be advantageously modeled by the homeomorphic regular self-similar (self-affine) fractals (see also Ref. 105).

Furthermore, it is emphasized that in some cases a brittle fracture surface (which possesses persistence scaling within the interval (17)) can be represented by self-similar pre-fractals, whereas the ductile fracture surfaces always display antipersistence behavior, and so they should be always treated as self-affine (or multi-affine) (pre)fractals.

Two variations of the Mandelbrot-Weierstrass function were suggested to statistically equivalent model representations of self-affine fracture surfaces with self-similar (isotropic) and self-affine (anisotropic) cross-sections.

It is shown that for (statistically) self-affine patterns the metric, information, and correlation dimensions are equal whereas $D_{\infty} \leq D_0 \leq D_{-\infty}$. The Eq. (31) for fractal dimension estimation from experimental data set is derived. The fractal properties of real fracture surfaces were analyzed on the base of experimental data reported in literature.

A new test of self-affinity (77) is proposed. Suggested theoretical concepts were validated by the analysis of graphs of Weierstrass function generated by the commercial program [79].

The possible reasons of strong contradictions between results of fractal measurements reported in different works were discussed on the basis of suggested concepts. Different methods of fractal measurement lead to the same fractal dimension only for a statistically self-similar fractal. Different methods of fractal measurement of the vertical cross-sections of a statistically self-affine fractal should give the same value of the roughness (Hurst) exponent, if they applied correctly. Multi-affinity of real fracture surfaces manifests itself in the difference between Hurst exponents estimated by different methods. Horizontal cross-sections in fracture surfaces are commonly statistically self-similar within the lengthscale interval (17). New relation (70) between fractal dimension of surface and the slope of the perimeter-area plot used in the slit-island fractal measurement is derived. It is noted that previously published data obtained by slit-island method should be revised with the use of Eq. (70).

The fractal properties of brittle fracture surfaces formed in steel 1045 fractured at different temperatures and different strain rates have been studied. Our data are in contradiction with the concept of universality of the fracture roughness exponent, which became popular in recent years. Moreover, it is noted that the changes in fractal properties of fracture surface coincide with changes in mechanical properties of steel.

ACKNOWLEDGMENTS

The courtesy and support of the staff and faculty of the Materials Research Center at ITESM, and especially the Chairperson Professor Armando Bravo, are gratefully acknowledged.

REFERENCES

1. E.E. Underwood and K. Banerji, in *ASM Handbook, V. 12: Fractography*, (The Materials Information Society, New York, 1992) 211.
2. R.W. Hertzberg, *Deformation and Fracture Mechanics of Engineering Materials*, (Wiley, New York, 1989).
3. V.S. Ivanova, A.S. Balankin, I.J. Bunin, and A.A. Oksogoev, *Synergetics and Fractals in Material Sciences*, (Nauka, Moscow, 1994).
4. A.S. Balankin, *Synergetics of Deformed Solids*, (Dep. Defense USSR Press, Moscow, 1992).
5. A.S. Balankin and P. Tamayo, *Rev. Mex. Fís.* **40** (1994) 506.
6. G.P. Cherepanov, A.S. Balankin, and V.S. Ivanova, *Eng. Fracture Mech.* **51** (1995) 997.
7. G.P. Cherepanov, A.S. Balankin, and V.S. Ivanova, in *Fracture: A Topical Encyclopedia of Current Knowledge Dedicated to Alan Arnold Griffith*, edited by G.P. Cherepanov (Krieger, Melborne, USA, 1996).
8. B.B. Mandelbrot, D.E. Passoja, and A.J. Paullay, *Nature* **308** (1984) 721.
9. A.S. Balankin, *Phys. Rev. B* **53** (1996) 5438.
10. A.S. Balankin, *Rev. Mex. Fís.* **41** (1995) 473.
11. A.S. Balankin, *Phys. Lett.* **A 210** (1996) 51.
12. A.S. Balankin, *Rev. Mex. Fís.* **42** (1996) 168.
13. A.S. Balankin and A. Bravo, in *Proc. I IUTAM Symposium on Micromechanics of Plasticity and Damage of Multiphase Materials*, Aug. 29 - Sept. 1, 1995, Paris, France (Kluver, London, 1996).
14. A.S. Balankin, *Sov. Tech. Phys. Lett.* **15** (1989) 878.
15. A.S. Balankin, A.A. Lubomudrov, and I.T. Sevrykov, *Sov. Phys. Tech. Phys.* **34** (1989) 1431.
16. A.S. Balankin, *Sov. Tech. Phys. Lett.* **16** (1990) 248.
17. A.S. Balankin, *Sov. Tech. Phys. Lett.* **17** (1991) 391.
18. A.S. Balankin and G.N. Yanevich, *Sov. Tech. Phys. Lett.* **17** (1991) 236.
19. A.S. Balankin and A.L. Bugrimov, *Sov. Tech. Phys. Lett.* **17** (1991) 630.
20. A.S. Balankin, *Sov. Tech. Phys. Lett.* **17** (1991) 531.
21. A.S. Balankin, *Sov. Tech. Phys. Lett.* **17** (1991) 229.
22. A.S. Balankin, *Sov. Tech. Phys. Lett.* **17** (1991) 632.
23. A.S. Balankin, *Dokl. Akad. Sci USSR* **322** (1992) 869.
24. A.S. Balankin and A.L. Bugriomov, *Polymer Sci.* **34** (1992) 246.
25. A.S. Balankin and A.L. Bugrimov, *Polymer Sci.* **34** (1992) 889.
26. A.S. Balankin, *Transactions of the U.S.S.R. Academy of Sciences: Earth Sci. Section* **319 A** (1993) 291.
27. A.S. Balankin, *Sov. Phys. Dokl.* **37** (1993) 379.
28. A.S. Balankin, V.B. Lazarev, and A.D. Izotov, *Inorganic Materials* **29** (1993) 375.
29. A.S. Balankin, *Rev. Mex. Fís.* **41** (1995) 147.
30. A.S. Balankin and A.D. Izotov, *Rev. Mex. Fís.* **41** (1995) 783.
31. A.S. Balankin, *Rev. Mex. Fís.* **42** (1996) 307.
32. X.G. Jiang, W.Y. Chu, and J.M. Xiao, *Eng. Fracture Mech.* **51** (1995) 805.
33. V.Y. Milman, R. Blumenfield, N.A. Stelmashko, and R.C. Ball, *Phys. Rev. Lett.* **71** (1993) 204.
34. K.J. Måløy, A. Hansen, E.L. Hinrichsen, and S. Rough, *Phys. Rev. Lett.* **68** (1992) 213.
35. J.J. Friel and C.S. Pandle, *J. Mater. Res.* **8** (1993) 100.
36. A. Imre, T. Pajkossy, and L. Nyikos, *Acta Metall. Mater.* **40** (1992) 1819.

37. S.R. Brown and C.H. Scholz, *J. Geophys. Res.* **90** (1985) 12575.
38. W.L. Power *et al.*, *Geophys. Res. Lett.* **14** (1987) 29.
39. Z.Q. Mu and C.W. Lung, *J. Phys. D: Appl. Phys.* **21** (1988) 848.
40. H. Xie and D.J. Sanderson, *Eng. Fracture Mech.* **50** (1995) 529.
41. A.R. Rosenfield, *Scr. Metall.* **21** (1987) 1359.
42. A.S. Balankin, V.S. Ivanova, and V.P. Breusov, *Sov. Phys. Dokl.* **37** (1992) 106.
43. Z.G. Wang, D.L. Chen, X.X. Jiang, S.H. Ai, and C.H. Shih, *Scr. Metall.* **22** (1988) 827.
44. L.E. Richards and B.D. Dempsey, *Scr. Metall.* **22** (1988) 687.
45. A.S. Balankin and V.S. Ivanova, *Sov. Tech. Phys. Lett.* **17** (1991) 12.
46. T.L. Anderson, *Scr. Metall.* **23** (1989) 97.
47. A.S. Balankin, *Sov. Phys. Solid State* **34** (1992) 658.
48. Ch. Lu and H. Xie, *Int. J. Fracture* **72** (1995) R55.
49. J. Schmittbuhl, J.P. Viotte, and S. Roux, *Phys. Rev. E* **51** (1995) 131.
50. A.S. Balankin, *News of Academy of Sci. of Russia, Ser.: Metals*, **N 2** (1992) 41.
51. F. Dossou and R. Gauvin, *Fractals* **2** (1994) 249.
52. B.B. Mandelbrot, *The Fractal Geometry of Nature*, (Freeman, New York, 1984).
53. J.M. Ziman, *Models of Disorder*, (Cambridge University, New York, 1979).
54. R.J. Adler, *The Geometry of Random Fields*, (Wiley, New York 1981).
55. R.F. Voss, *Scaling Phenomena in Disorder Systems*, (Plenum Press, New York, 1985).
56. M.V. Berry and Z.V. Lewis, *Proc. R. Soc. London, Ser.* **A 370** (1980) 459.
57. M. Giona, *Chaos, Solitons & Fractals* **5** (1995) 987.
58. J. Feder, *Fractals*, (Plenum Press, New York, 1988).
59. J.M. Fuchs, *Izv. Vuzov, Ser. Radiophysics* **26** (1982) 1194.
60. P. McAnulty, L.V. Meisel, and P.J. Cote, *Phys. Rev. A* **45** (1992) 3523.
61. A. Hansen, E.L. Hinrichensen, K.J. Måløy, and S. Roux, *Phys. Rev. Lett.* **71** (1993) 205.
62. J. Kertész, V.K. Horváth, and F. Weber, *Fractals* **1** (1993) 67.
63. A.S. Balankin, *Eng. Fracture Mechanics*, Special issue *Statistical Fracture "Mechanics"*, **1** (1997) 1.
64. B.B. Mandelbrot, in *Fractals in Physics*, edited by L.Pietronero and E.Tosatti (Elsevier, New York, 1986) 3.
65. E. Bouchaud, G. Lapasset, and J. Planés, *Europhys. Lett.* **13** (1990) 73.
66. E. Bouchaud and S. Navéos, *J. Phys. I France* **5** (1995) 547.
67. P. Meakin, *Science* **252** (1991) 226.
68. P. Meakin, *Phys. Rep.* **235** (1993) 189.
69. A. Chudnovsky, *J. Appl. Phys.* **62** (1987) 4124.
70. D. Jeulin, *Eng. Computations* **10** (1993) 81.
71. A.S. Balankin and A.L. Bugrimov, in *Abstracts XXVIII Int. Congr. on Theoretical and Applyed Mechanics, Haifa, Israel, 22-28 August 1992* (IUTAM Press, Haifa, 1992), p. 17.
72. V.B. Lazarev, A.S. Balankin, and A.D. Izotov, *Inorganic Materials* **29** (1993) 883.
73. P. Grassberg and I. Procaccia, *Physica* **D 9** (1983) 189.
74. A.L. Barabási, P. Szépfalusy, and T. Vicsek, *Physica* **A 178** (1991) 17.
75. A.L. Barabási and T. Vicsek, *Phys. Rev. A* **44** (1991) 2730.
76. R. Badii and A. Politi, *Phys. Lett.* **A 104** (1984) 303.
77. R. Badii and A. Politi, *Fractals in Physics*, edited by L.Pietronero and E.Tosatti (Elsevier, New York, 1986) 636.
78. J.G. Moreira, J.K.L. Silva, and S.O. Kamphorst, *J. Phys. A* **27** (1994) 8079.
79. *Fractal Vision Software and Bonus Programs*, by Dick Oliver Cedar, Software (1992).

80. R.H. Dauskardt, F. Haubensak, and R.O. Ritchie, *Acta Metall. Mater.* **38** (1990) 143.
81. S. Kulback, *Information Theory and Statistics*, (Nauka, Moscow, 1967).
82. L.D. Landau and E.M. Lifshiz, *Statistical Physics*, Part 2 (Pergamon Press, Oxford, 1978).
83. A.S. Balankin, *Int. J. Fracture* **76** (1996) R63.
84. V.M. Sith and S.C. Lim, *J. Phys. A* **28** (1995) 2995.
85. B. Nowicki, *Wear* **102** (1985) 161.
86. T. Engøy, *Phys. Rev Lett.* **73** (1992) 834.
87. A. Hansen, T. Engøy, and J. Måløy, *Fractals* **2** (1994) 527.
88. M. Sahimi, *Rev. Mod. Phys.* **65** (1993) 1395.
89. B.L. Cox and J.S.Y. Wang, *Fractals* **1** (1993) 87.
90. D.V. Pisarenko and V.F. Pisarenko, *Phys. Lett.* **A 197** (1995) 31.
91. A. Neimark, *Physica* **A 191** (1992) 258.
92. *Fractals in Science*, edited by A. Bunde and S. Havlin (Springer-Verlag, New York, 1994).
93. A. Imre, T. Pajkossy, and L. Nyikos, *Acta Metall. Mater.* **40** (1992) 1892.
94. K. Falconer, *Fractal Geometry: Mathematical Foundations and Applications*, (Wiley, New York, 1990).
95. B.L. Cox and J.S.Y. Wang, *Fractals* **1** (1993) 547.
96. E.E. Underwood and K. Banerji, *Mater. Sci. Eng.* **80** (1986) 1.
97. L. Smith, *Phys. Lett.* **A 133** (1988) 283.
98. D. Ruelle, *Proc. R. Soc. London, Ser. A* **427** (1990) 241.
99. A.A. Tsonis and J.B. Elsner, *J. Stat. Phys.* **81** (1995) 869.
100. W.F. Smith, *Fundamentos de la Ciencia e Ingenieria de Materiales*, (McGraw-Hill, México, 1993).
101. H.E. Davis, G.E. Troxell, and G.F.W. Hauck, *The Testing of Engineering Materials*, (McGraw-Hill, New York, 1982).
102. S. Kyriacos, S. Buczkowski, F. Nekka, and L. Cartilier, *Fractals* **2** (1994) 321.
103. A.S. Balankin, *Philosophical Magazine Letters* **74** (1996) 415.
104. A.S. Balankin, A. Bravo, M.A. Galicia, and O. Susarrey, *Int. J. Fracture* **79** (1996) R63.
105. A.S. Balankin and O. Susarrey, *Int. J. Fracture* **81** (1996) R27.